TÉCNICO LISBOA

# Mobility Characterization and Dynamical Analysis of a Surface Hopper for Low-gravity Environments

**Miguel Borges Pinheiro**

Thesis to obtain the Master of Science Degree in

## Aerospace Engineering

Supervisors: Prof. Rodrigo Martins de Matos Ventura
Prof. João Manuel Gonçalves de Sousa Oliveira

### Examination Committee

Chairperson: Prof. Paulo Jorge Coelho Ramalho Oliveira
Supervisor: Prof. Rodrigo Martins de Matos Ventura
Member of the Committee: Prof. António Pedro Rodrigues de Aguiar

**January 2021**

Aos meus pais.

# Acknowledgments

A word of appreciation to my supervisors at Técnico Lisboa – Professors Rodrigo Ventura and João Oliveira – for their orientation and for the opportunity of working on this topic.

My sincerest gratitude to Dr. Benjamin J. Hockman from NASA Jet Propulsion Laboratory and lead engineer on the “Hedgehog” project at Stanford University, for the insightful discussion and advice over the topic and work of this thesis.

I would like to thank my family and friends who were part of this journey. Particularly to my good friend and colleague Daniel Pinto for sharing his thoughts about my work. And to my girlfriend for her continuous support and motivation.

And with the most important for last, I would like to thank my parents for their continuous unconditional support throughout the duration of my degree.

# Resumo

O crescente interesse científico na exploração de corpos celestes de baixa gravidade, como cometas, asteróides, ou pequenos satélites planetários, criou uma maior necessidade de missões de mobilidade na superfície. Os sistemas de salto com atuação interna fornecem uma opção eficiente e viável para obter mobilidade na superfície deste tipo de ambientes, e com baixo custo operacional. Um sistema de atuação recorrendo a volantes de inércia, permite um elevado controlo e flexibilidade de design. Através de manobras de auto-correção, menos atuadores são necessários e um movimento mais simples de salto sobre um único eixo paralelo pode ser alcançado. Nesta tese, é estudada a mobilidade de salto do rover com base nas referidas configurações.

A análise dinâmica e as simulações realizadas forneceram conclusões importantes, que resultaram em propostas inovadoras de aplicações que mostram melhorias significativas nas operações do rover e na distância de salto alcançada para diferentes inclinações da superfície. É demonstrado o interesse de aplicar uma configuração dos suportes de locomoção de ângulo variável e de comprimento variável. A implementação de suportes que podem ajustar e controlar o seu ângulo melhora significativamente a distância de salto alcançada para diferentes inclinações da superfície. Suportes de comprimento variável permitem funcionar como uma ferramenta de balanço entre saltos mais eficientes, com suportes mais curtos, e uma melhor capacidade de ultrapassar obstáculos através de suportes mais longos. Esta variação de comprimento apresenta principalmente uma contribuição com potencial para a fase de aterragem, contudo, estudos adicionais desta aplicação são necessários.

**Palavras-chave:** Mobilidade, Rover, Dinâmica de Salto, Exploração de Corpos Menores, Configuração de Suportes de salto

# Abstract

The growing scientific interest in the exploration of low-gravity celestial bodies, such as asteroids, comets, or small planetary satellites, has developed a higher need for mobile surface missions. Internally-actuated hopping systems provide an efficient and viable opportunity to achieve surface mobility under such environments, with low operational cost. The rover's actuation using flywheels, implements a high control, design flexibility, and enclosed mobility mechanism. Through self-righting maneuvers, fewer actuators are needed and a simpler single-axis hopping motion can be achieved. Throughout this thesis, the rover's hopping mobility based on these configurations is studied.

The dynamical analysis and simulations performed provided important conclusions, and innovative new applications are proposed that show significant improvement on the hopper's operation and on the hop distance achieved for different surface inclinations. It is showed the interest of applying a variable spike angle configuration and a variable spike length configuration. The application of a spike that can adjust and control its angle improves significantly the hop distance achieved for different surface inclinations. The implementation of a spike that can change its length works as a trade-off solution between more efficient hops with shorter spikes and better transverse capability over higher obstacles with longer spikes. This later variation presents particularly a potential contribution to the landing stage, however a further study of this application is needed.



**Keywords:** Mobility, Rover, Hopping Dynamics, Small Body Exploration, Spike configuration

# Contents

# List of Tables

# List of Figures

# Nomenclature

### Greek symbols

| | |
|---|---|
| $\alpha$ | Angle of the spike. |
| $\beta$ | Surface inclination angle. |
| $\eta$ | Efficiency. |
| $\omega_f$ | Flywheel angular speed. |
| $\overline{\tau}$ | Constant Torque. |
| $\tau$ | Torque. |
| $\theta$ | Angle between the stance spike and the vertical. |
| $\mu$ | Friction coefficient. |
| $\rho$ | Density. |
| $\epsilon$ | Relative tolerance. |
| $\omega$ | Angular speed. |
| $\phi$ | Impact inclination angle. |

### Roman symbols

| | |
|---|---|
| $G$ | Newton's gravitational constant. |
| $g$ | Gravitational acceleration. |
| $r_{body}$ | Body's radius. |
| $v_{esc}$ | Escape velocity. |
| $a$ | Linear acceleration. |
| $d_h$ | Horizontal hop distance. |
| $l$ | Spike's length from center of mass. |
| $m$ | Mass. |

$v$ Linear velocity.

$I_f$ Flywheel's rotational inertia.

$I_r$ Rover's rotational inertia.

$R$ Surface reaction force.

$D$ Dissipative energy.

$M$ Momentum.

$T$ Kinetic energy.

$V$ Potential energy.

$C$ Surface damping.

$K$ Surface stiffness.

$e$ Coefficient of restitution.

$F_c$ Impact force.

$F_N$ Contact force.

$P$ Impulse.

$r_c$ Position vector of the contact point.

**Subscripts**

$h$ Hopping instant.

$i, j, k$ Computational indexes.

$N, n$ Normal component.

$T, t$ Tangential component.

$x, y$ Cartesian components.

**Superscripts**

-1 Inverse matrix.

. Derivative with respect to time.

.. Second derivative with respect to time.

- Before event.

+ After event.

# Chapter 1

# Introduction

This thesis targets the space exploration field, more particularly in small body missions for surface exploration and investigation through mobile rovers. The characterization of the mobility system and the locomotion dynamics are an important component to be studied for the development of such rovers.

## 1.1 Motivation

The exploration and investigation of small celestial bodies such as small planetary satellites, asteroids, and comets, have been increasing in the last years. These objects may enable to better explain the origin of the universe and the evolution of the solar system. It is believed that some of these small bodies have been minimally altered from the initial state in which the planets were formed [1]. Missions conducted to study asteroids and comets were successful to establish the current understanding of their evolution, characteristics and composition. However, much more investigation is required to fully understand and study these small bodies.

Mobile rovers are specially interesting for the exploration of this small celestial targets as they can move through the surface and perform important operations that allow the better understanding and characterization of these space objects. Among this operations are: soil and surface characterization, mapping the terrain, sample extraction, periodic behavior analysis, image capture and other sensor readable features, such as temperature, vibration and others. Their small size and low investment funds needed are very attractive characteristics and could grant the possibility of future missions where several of this robots work together simultaneously.

The mobility of such rovers on these celestial bodies has been a challenge and a current focus of investigation, with several different approaches and developed projects. The biggest obstacles of these missions are the complex and varying surface composition and the micro-gravity environment that make surface mobility very challenging.

Although important progress has been made in this field in the recent years, many obstacles and uncertainties are still present in the performance of micro-gravity rovers.

## 1.2 Topic Overview

Small bodies are celestial objects with small sizes and very low gravity levels. They include small planetary satellites, asteroids, comets, the objects in the Kuiper Belt and the Oort cloud, Triton, Pluto, Charon, and interplanetary dust. Comets and asteroids are believed to be remnants from the formation of the solar system. Their surface is particularly characterized by its complexity and irregularity, with craters, uneven shape and extremely rocky areas. The surface is composed by varying soil characteristics from comprised minerals, rigid rocks and ice, to soft surfaces and loose regolith. Small planetary satellites, comets and asteroids have been the main targets of scientific missions in the last years.

One of the first missions to explore small bodies was conducted by the Soviet Union on July 12, 1988. The spacecraft Phobos 2 was launched with the objective to examine the Martian moons Phobos and Deimos [2]. The mission was to perform, after several correction maneuvers, an approach to the surface of Phobos at approximately 50 meters, which represented a high proximity compared to the previous 100 kilometer distance of Viking 1 passage [3]. This would allow to capture high-spectral-resolution images of the surface, study the composition of the regolith, and to release two small probes on Phobos' surface. One of these was the PrOP-F Phobos hopping rover [4], that used spring-loaded legs and a reorientation mechanism, as shown in Figure 1.1. Several important measurements were obtained by Phobos spacecraft, but unfortunately the lander's mission was not successful due to communication loss with the spacecraft. However, this served as inspiration for future missions.

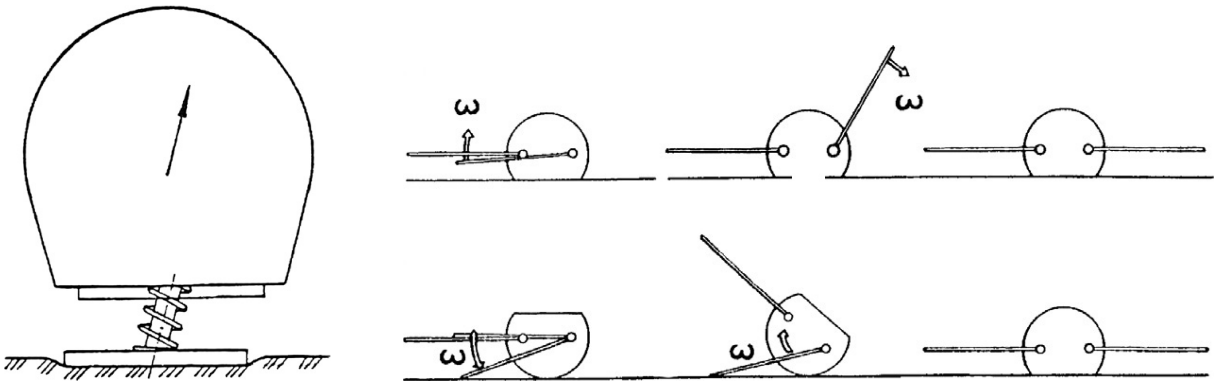


(a) Hopping concept (b) Reorientation concept

Figure 1.1: PrOP-F Phobos hopper concept [4]

The vast history of comets observations dates back to the prehistoric man. Being visible from earth and by the naked eye, it is not surprising the early interest in space missions to target this celestial small bodies. Several missions were conducted between 1984 and 1986 to Halley's comet. Giotto spacecraft, from the European Space Agency (ESA), was the first to capture an image of Halley's comet nucleus in 1986. And by the probe HOPE aboard this spacecraft, performed the first measurements of the dust properties inside the comet [5]. In 2005, NASA launched the Deep Impact mission targeting the Temple-1 comet, which was the first provided important data and information about the comets characteristics and composition [6]. In 2006, NASA's mission Stardust to Wild 2 was able to return the first samples from a comet [7].

In more recent years, ESA's Rosetta mission to the 67P/Churyumov-Gerasimenko between 2014 and 2016 represented one of the most important missions to a comet, gathering important information and notable measurements of this type of space objects [8]. The Philae lander was released from the spacecraft into the surface of the comet in order to provide valuable readings of the soil characteristics [9]. Upon initial contact with the surface, Philae was intended to anchor itself on the ground, however, due to a malfunction of the mechanical anchoring system the contact with the surface lead to unintentional bounces across the surface, as shown in Figure 1.2(b). Although accidental, the Philae's hop is currently the only ever executed on a comet's surface. The motion raised interesting aspects involving the dynamics of comet surfac mobility [10]. Observations revealed that the lander approach the surface at approximately 1 m/s and bounced with a rebound velocity of 30 cm/s, which resulted in a 1.2km distance covered. When it came to rest the lander was still functional.

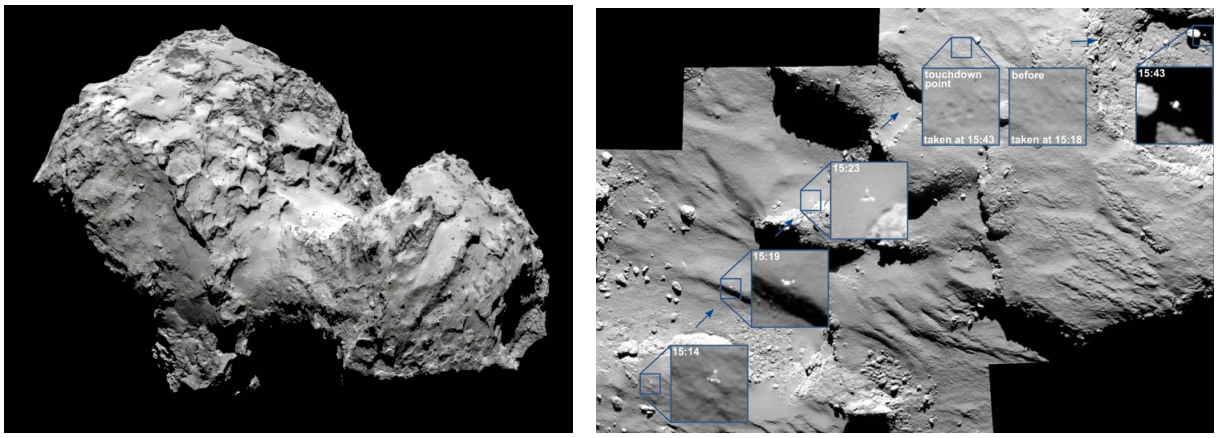


(a) Comet 67P/Churyumov-Gerasimenko

(b) Philae flight path on the surface

Figure 1.2: Images from the Rosetta mission to comet 67P/Churyumov-Gerasimenko. (image courtesy of ESA, rosetta.esa.int)

The observation of asteroids in history is far more recent than the comets. It was only by the nineteenth century that the existence of the asteroid 'belt' between Jupiter and Mars orbits was discovered. Since then, the scientific interest in this small bodies has increased exponentially. The Galileo probe was the first to provide a close image of an asteroid, in 1991 [11]. In 2001, NASA's spacecraft NEAR-Shoemaker completed the landing on asteroid 433 Eros. The mission provided investigation data on the magnetic field, mass distribution, and composition of the asteroid [12].

The Japan Aerospace Exploration Agency (JAXA) has been one of the biggest contributors for asteroid's investigation and exploration. Through the mission Hayabusa to asteroid (25143) Itokawa in 2005, JAXA was able to perform the first successful sample return from an asteroid [13]. The Hayabusa spacecraft was launched in May 2003 and arrived to the target in September 2005. First, the spacecraft performed mapping and imaging operations while orbiting the asteroid for over a month. Secondly, while practicing descent maneuvers, it released a small hopper called MINERVA, represented in Figure 1.3, to perform surface mobility operations [14]. However, due to an error the probe release trajectory was not perform correctly, which resulted in MINERVA missing the asteroid.

The Hayabusa spacecraft completed two touchdowns on the surface, with the second one resulting

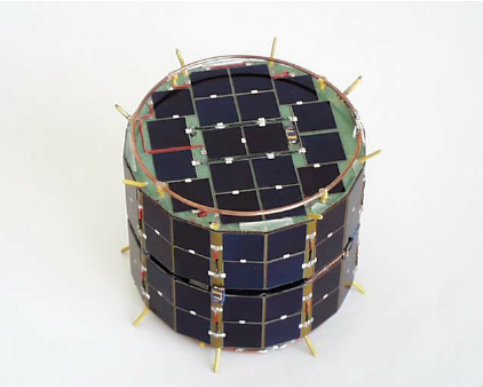

Figure 1.3: Hayabusa MINERVA hopper [14].

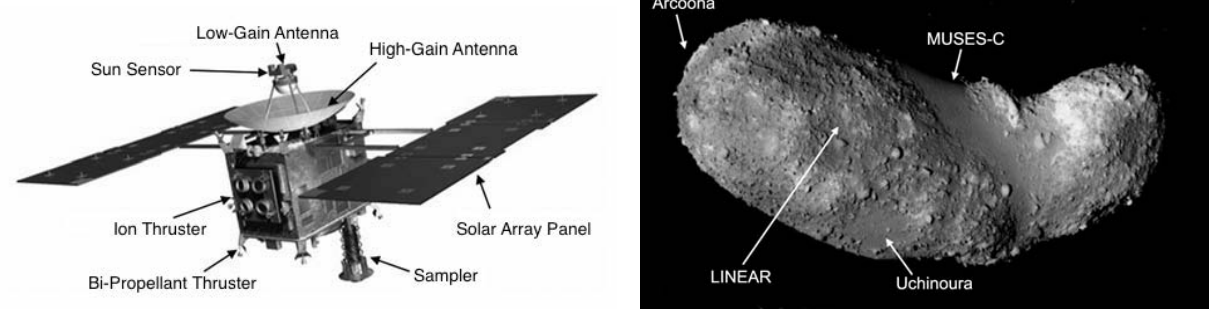


(a) Hayabusa spacecraft

(b) Itokawa asteroid captured from Hayabusa

Figure 1.4: Hayabusa spacecraft and target asteroid Itokawa [13].

in a successful sample extraction. In Figure 1.4 it is possible to see the Hayabusa spacecraft and an image captured of the target asteroid, with the touchdown area located near MUSES-C. After several complications the spacecraft was able to return to Earth in 2010, with the extracted samples of the asteroid's surface. Very important information on the composition and origin of these small bodies was obtained from the samples' analysis. The success of this mission served as catalyst for asteroid exploration.

On December of 2014, JAXA launched Hayabusa2 spacecraft that in 2018 arrived to the target asteroid 162173 Ryugu, formally known as 1999JU3. Similar to the first mission, the spacecraft performed in-orbit operations for shape, mass, and geomorphology observations, and through it determine a suitable sample site. The mission was also successful in the collection of samples from the asteroid's surface and deeper underground particles inside the asteroid [15].

On board of the Hayabusa 2 there were three small MINERVA-II robots developed by JAXA and Tohoku University, and one small lander developed by the German Aerospace Center (DLR) called MASCOT. The rovers were released in different regions of the asteroid to perform sensor reading operations, image capturing, and hopping mobility across the asteroid's surface [16]. The MINERVA-II autonomous hoppers successfully performed hops on the surface and were able to establish communication with the spacecraft, being the last signal received after 10 months on the ground. They constitute the first ever mobile rovers to operate successfully on a small body.

The MASCOT rover had a primary battery with an active 17 hour lifetime, and was successful in its

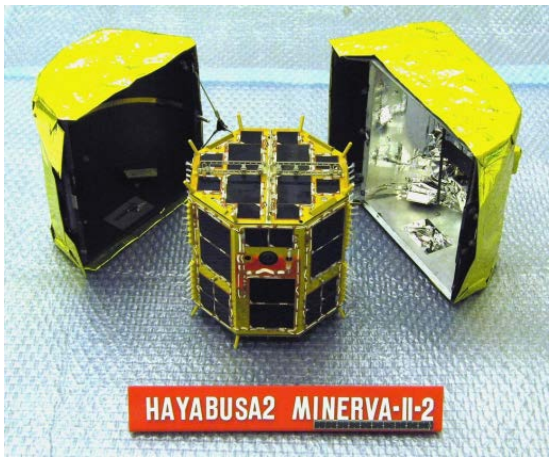


(a) MINERVA-II-2 hopper

(b) MASCOT lander

Figure 1.5: Hayabusa2 onboard hoppers for Ryugu asteroid surface exploration.

data obtaining mission and on performing a commanded hop by the operation center [17]. In Figure 1.5 one MINERVA-II hopper and the MASCOT lander are represented.

Currently, a microgravity hopper called Hedgehog – developed by the Department of Aeronautics and Astronautics of Stanford University working alongside with the NASA Jet Propulsion Laboratory (JPL) and the Massachusetts Institute of Technology (MIT) – is one of the most promising projects and concept missions in the field of mobility rovers for small body surface exploration. The Hedgehog hopper is currently in Phase II of NASA Innovative Advanced Concepts (NIAC) program [18]. This hopper is presented in more detail in section 2.2.4. The prototype evolution of the Hedgehog throughout the years can be seen in Figure 1.6.

(a) 1st prototype

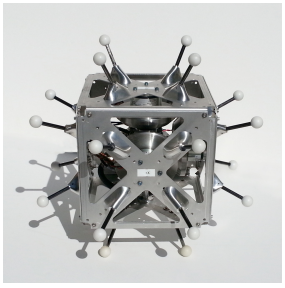

(b) 2nd prototype

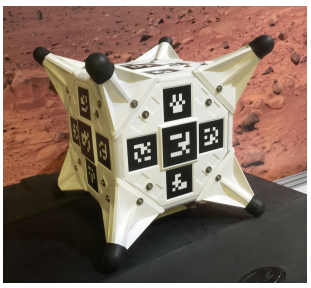

(c) 3rd prototype

(d) Current hopper design

Figure 1.6: Evolution of the Hedgehog hopper prototypes.

## 1.3 Objectives

The objective of this thesis was to select and study a replacing mobility design for the Moon Hopper rover developed at the Institute for Systems and Robotics, Lisboa, with the purpose of altering his target missions to the recent grown interest of the space exploration field of the Solar System Small Bodies. The system used by the referred Moon Hopper was a hopping mechanism similar to the Canadian Space Agency (CSA) micro-planetary hopping rover [19], (see Figure 2.4(c)). Considering the recent

advances in the rover development investigation for surface operations on this type of celestial bodies, the thesis main objective is focus on a rover mobility characterization and a first-order dynamic analysis for locomotion on the surface of small bodies with micro-gravity environment.

This thesis, throughout a literature overview and theoretical background, intents to define and select the core configurations and design for the mobility rover, model the rover's motion and perform a dynamic analysis of the mobility system. The objective to describe the contact dynamics with the surface throughout the rover's motion, and identify potential changes and improvements to the selected configuration. Perform simulations of the rover's mobility to understand the influence of the gravity levels for the viability of the mobility system, and the impact of the design parameters.

In addition to the aforementioned, the ambition of the work developed in this thesis is to propose a innovative configuration or idea for the rover surface mobility that represents a contribution for the field.

## 1.4 Thesis Outline

This thesis is divided in five chapters, detailing the important stages of the work developed.

In the first chapter the work objectives and topic are introduced. An overview on the history and previous missions of small-body investigation and their surface exploration are presented. And the main objectives and motivation for this work are outlined.

Chapter two addresses the first step to characterize the mobility system. Essential notions on the environment and mobility configurations that must be considered before the rover motion dynamics can be studied. It includes the gravity levels and escape velocity from the target body, and possible mobility designs and configurations for the surface exploration rover's locomotion.

Chapter three represents the motion dynamics of the rover. First, the motion assumptions and the dynamic considerations are established. The several phases of motion for the hopping are described and modelled, with all the hopping conditions and two different flywheel braking approaches considered. Later in the chapter, the contact dynamics are studied for both the contact motion performed with continuous contact with the surface, and the impact stage at landing. The motion dynamical analysis obtained throughout this chapter will provide the equations and conditions for the numerical model and simulations performed and discussed in the following chapter.

Chapter four consists of the numerical model applied and the results obtained from the simulations, as well as the discussion of the aforementioned. First, the numerical method applied is described. The resulting simulations for the studied scenarios and conditions are presented and discussed. In a last section of this chapter new and innovative proposed configurations to be implemented in the rover design are specified.

The final chapter includes the final conclusion remarks and the resulting future work to be studied.

# Chapter 2

# Background

This chapter introduces concepts needed to describe and study the rover's mobility system and surrounding environment. Important notions and configurations must be considered and selected before the rover dynamics are studied. Namely, the gravity levels and escape velocity range inherent to the small-body environments, and the rover mobility possible configurations and design.

## 2.1 Gravity Levels and Escape velocity

The small bodies of the solar system are well-known for their low gravitational fields. Because of that, for any surface exploration or mobility it is very important to considered the very low escape velocities present. Beyond that, their irregular shape and distribution of mass gives them irregular gravity levels along the surface, specially on smaller asteroids and comets.

Very few small bodies from the known database [20] of our solar system have been studied or explored. And even less have their surface characteristics and physical properties confirmed. The local gravity at the surface is mainly estimated through complex models and known dimension and density data. However, if the body's dimension and density are considered homogeneous, the mean gravitation for the small body's surface can be calculated:

$$g_{body} = G \cdot \frac{m_{body}}{r_{body}^2} = G \cdot \frac{4}{3}\pi\rho \cdot r_{body} \tag{2.1}$$

In which $G$ represents the Newton's gravitational constant, $\rho$, $m_{body}$ and $r_{body}$ the small body's density, mass and radius, respectively. From asteroids and comets to small planetary satellites, this represents very low gravitation levels on the range of $10^{-5}$ to $10^{-3}[m/s^2]$. Resulting in extremely low contact forces at the surface with any exploration object, and therefore very low escape velocities, approached by Equation 2.2, that can range between 0.02 to 2 [m/s].

$$v_{esc} = \sqrt{\frac{2 \cdot G \cdot m_{body}}{r_{body}}} = r_{body}\sqrt{\frac{8}{3}\pi \cdot G \cdot \rho} \tag{2.2}$$

It is extremely important that all operations performed on the surface respect with margin the escape

velocity bound. In table 2.1 are listed some estimated mean gravitation and escape velocity parameters of relevant small bodies [20].

| Target | $g\ [m/s^2]$ | $v_{esc}\ [m/s]$ |
|---|---|---|
| Phobos | $5.8 \times 10^{-3}$ | $11.35$ |
| 25143 Itokawa | $8.76 \times 10^{-5}$ | $0.17$ |
| 162173 Ryugu | $1.5 \times 10^{-4}$ | $0.39$ |

Table 2.1: Approximate mean gravitation and mean escape velocities from relevant small bodies.

For the dynamic analysis performed throughout this thesis, in Chapter 3, the small-body's close gravitational dynamical environment and the small-body's revolution attitude and rotation will not be taken into account, considering the purpose is to study the mobility system in a local referential and not the aforementioned interactions.

## 2.2 Rover Configuration and Design Considerations

Here the main configurations and design consideration for the mobile rover are discussed. From the core locomotion type, the shape and mobility actuation approach, to the structural characteristics. Lastly, the final core configurations are selected for the rover studied in the next chapters.

### 2.2.1 Types of Locomotion

Several locomotion types were proposed and used in space exploration rovers over the years, as mentioned in Section 1.2. The mobility around celestial objects can be categorized into friction-based or not friction based locomotion. On the second one, no contact with the surface is needed, which can be achieved by tethered robots or flying rover with jet thrusting propellant. In this thesis only friction-based mobility is studied. In this category, there are wheeled based rovers, leg-type robots, and hopping rovers. A different type of locomotion by floating mobility through electro-magnetic levitation was also proposed by Nakamura et al. [21], but the results showed very low achieved velocities.

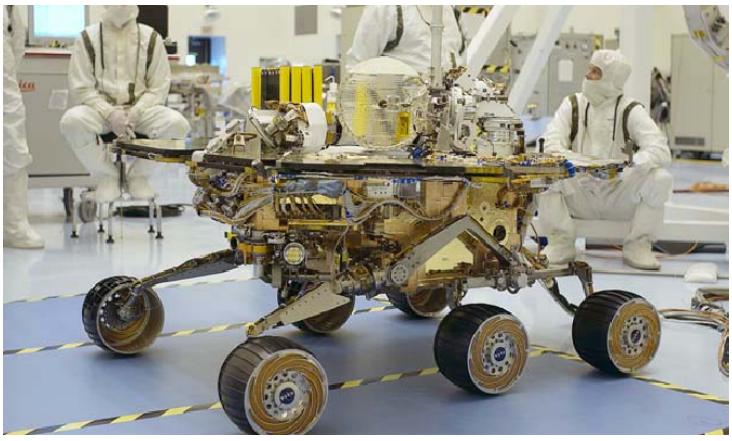

Figure 2.1: Mars Exploration Rover of NASA with wheeled locomotion used [22].

Wheeled rovers have had great success for surface operations and mobility on planets and moons, as the examples of Apollo Lunar Roving Vehicle [23] and Mars Exploration Rover [22], both developed by NASA. However, due to the extremely irregular surface and micro-gravity presence on small bodies, the wheeled rovers are not viable for the exploration of such targets. An example of a wheeled-type rover is shown in figure 2.1. Wheeled rovers use exclusively friction as way of locomotion. On friction-based mobility the forces acting between the rover and the target body's surface are strongly dependent on the contact force. The horizontal movement is driven by the traction force, which is obtained by the friction between the rover and the ground. According to the Coulomb's law, the driving force is given by:

$$0 \leq F_f \leq \mu F_N \tag{2.3}$$

Where $\mu$ is the surface friction coefficient, and $F_N$ the contact force between the rover and the surface. In wheeled mechanisms the normal contact force relies only on its mass and on the gravity:

$$F_N = mg \tag{2.4}$$

With $m$ being the rover's mass and $g$ the gravitational acceleration on the surface. Therefore, the driving force is proportional to the gravity acceleration. On small bodies, where $g$ is approximately between $10^{-5}$ and $10^{-3}[m/s^2]$, the friction force available for wheeled robots is extremely low. In conclusion, acceleration on the horizontal direction it is almost impossible to be achieved by the wheeled mobility mechanisms on small bodies, as previous studies show [24].

Another locomotion method that uses friction is the leg-type mobility, which mimics walking and can exert a higher pushing force on the ground than in proportion to its own weight. An example of a leg-type locomotion proposed rover is illustrated in Figure 2.2.

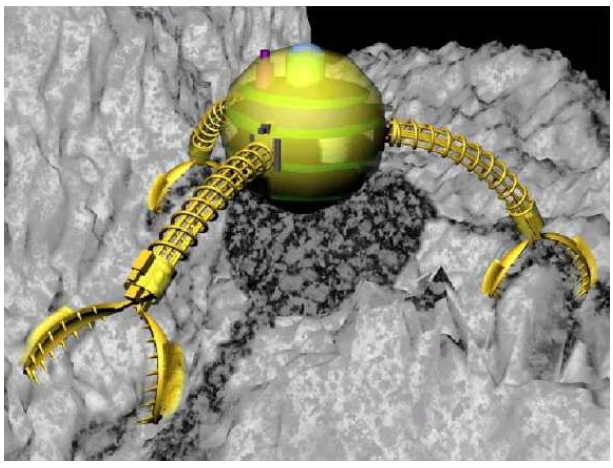

Figure 2.2: Leg-type mobility robot from Tohoku University [25].

The significant problems with this type of locomotion are its complex actuation and driven mechanisms, together with the high mission duration to transverse long distances. These mechanisms also rely on the surface characteristics that are usually highly unknown, which can result in anchoring challenges, as displayed by Philae's landing on the comet resulting in a unintentional jump [26]. For the reasons

aforementioned this type of locomotion does not indicate a viable way of mobility for small celestial bodies. The rock gripping mechanism implemented by Yuguchi et al. [25] presents an interesting attribute to solve the potential problem of the inoperable and *transversable* regions due to the gravity fluctuations on some asteroids and comets surface as introduced by Hockman and Pavone [27], although this mechanism can be adapted to be used in other more reliable mobility systems.

Finally, hopping is the type of locomotion most used in small body's exploration missions [4, 16, 17] and with more viable proposals throughout the years [28–32]. Hopping is a type of mobility that also uses friction as method of locomotion. However, unlike the wheeled mobility there is no constant contact with the surface and the friction acts in a short period, between the actuation of the jump process until the rover's take-off from the surface. Therefore, it also uses a different principle from the wheeled mobility to obtain the contact force, since there is an artificial pulling force applied against the surface to make the rover hop. In contrary to other locomotion types, hopping systems use the low-gravity presence as an advantage. Defining $F_h$ as the force applied to the ground by the hopping rover, the contact force on Equation 2.3 is:

$$F_N = (mg + F_h) \tag{2.5}$$

So even with extremely low gravity levels tending to zero, the hopping rover, from now on referred as hopper, can assure mobility. The driving force that can be used under microgravity from friction is:

$$F_f \leq \mu F_h \tag{2.6}$$

By controlling the pushing force it is possible to control the magnitude of the hopper's velocity, always limited by the target's escape velocity. The required hop speed and hop angle must be controlled with the hopper on the ground.

The hopping locomotion has been proven as the most efficient, suitable and adequate way of mobility under microgravity environment and conditions of the small bodies [33–35]. This is the selected type of locomotion to be used in this work.

### 2.2.2 Hopping Methods and Mechanisms

Different principles and concepts can be used to perform surface mobility by hopping. There are three main principles: *thruster*, repulsion and *torquer* mechanisms. Repulsion mechanisms include elastic and striking methods, with the later referring to hitting the surface with a movable arm or part. Repulsion and torquer mechanism principles are illustrated in Figure 2.3 and their overall advantages and disadvantages are presented in this section.

Mechanisms using thrusters and propellant as principle of mobility offer largest hopping distances, however, their thrusting system is heavy and operationally complex. They are limited to a finite number of hops, and they represent a possible surface contamination agent. In addition, the low-gravity environment does not require such high thrusting force to perform surface hops. Following the sustainable and low-cost efficiency requirements for this field of study, this type of mechanisms are not feasible for small

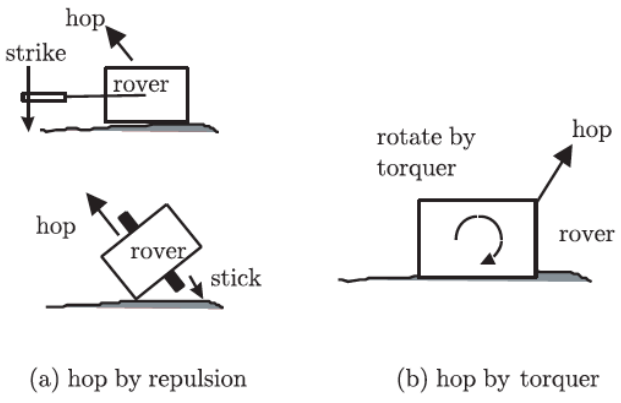


Figure 2.3: Hopping methods [36].

body hoppers.

Elastic and striking based mechanisms on the other hand provide virtually ”infinite” number of hops and a simpler system approach. This type of mobility was the first to be used in in-situ missions to small bodies (see Figure 1.1), although no data was retrieved from the hopper's mobility mechanism performance on the surface [2]. Several configurations using an elastic based mechanism were proposed throughout the years for planetary and Moon surface mobility [19, 28, 29, 37, 38], as shown in Figure 2.4. The most common configuration lays upon a spring compression mechanism for hopping. After the hop is concluded a self-righting mechanism needs to re-position the hopper in order to perform another hop.

The elastic-based method of hopping represents an abrupt and impulsive actuation which results in a poor control capability of the hop angle and velocity. Also, considering that to perform a hop the rover needs to have the right attitude on the surface it does not represent an admirable adaptability to the irregular terrain.

Torquer hoppers use internally-actuated torque to rotate the hopper and produce a reaction force against the surface to make the platform hop. The thrusting force obtained is much smaller than the spring-based hoppers, which might represent a complication for the mobility on the Moon and Mars gravity levels, where a too powerful and heavy torque is needed. However, this is not a problem for microgravity environments where the torques needed are significantly much lower. This hopping principle has been widely applied in mobility rovers for surface exploration of small bodies [32, 39, 40]. The main advantage of this type of hoppers is the high control ability provided to the rover's motion. It also possesses higher adaptability to the uneven terrain in comparison to other hopping principles. Since the actuator is inside the body, it is protected against contamination by potential dusts that might be part of the surface. The torquer can also be used to perform attitude control during the hop flight, execute tumbling motions, or to posture the hopper in the right direction to perform the following hop.

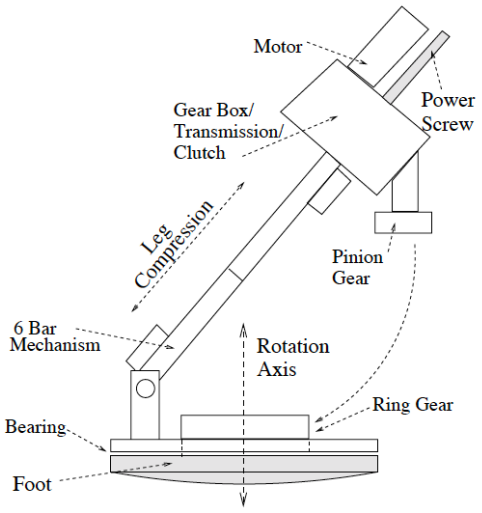


(a) JPL second generation hopper

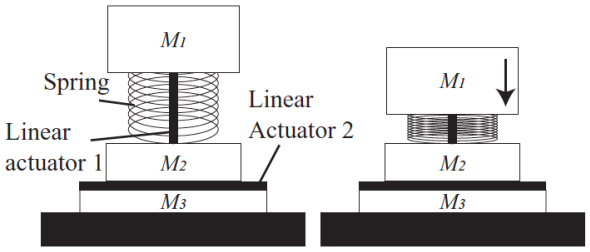


(b) JAXA's hopper alternative proposal

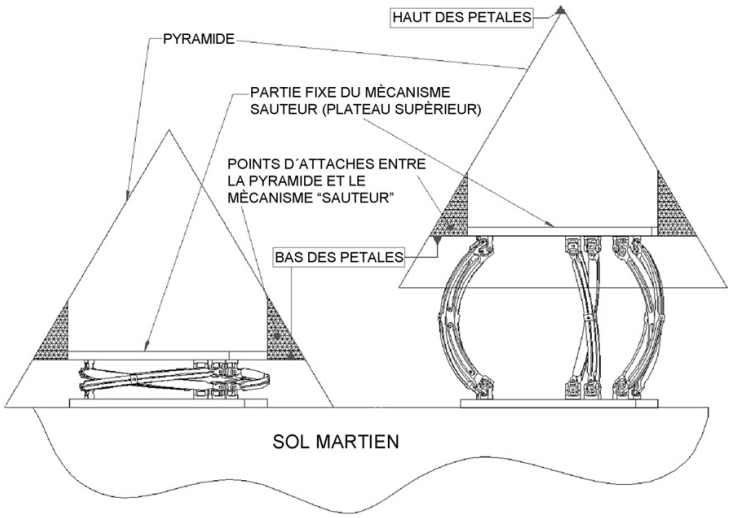


(c) CSA micro-planetary hopper

Figure 2.4: Spring-based mobility rovers. a: [29], b: [28], c: [19]

### 2.2.3 Configurations of Torquer Hoppers

Different configurations can be implemented for the torquer mechanism. The MASCOT hopper, developed by the German Aerospace Center (DLR), uses an internal eccentric arm driven by a brushless DC motor [41]. While the rover is on the ground, by accelerating and decelerating the arm in a rotating motion, a defined torque is applied on the hopper by the resulting reaction force. This mechanism allows hopping and self-righting maneuvers in different directions. The mobility mechanism system design is illustrated in Figure 2.5.

Other more used *torquer* methods have been implemented with orthogonal DC motors attached with a mass on a momentum wheel (i.e. a flywheel as a comprised disk [42]). A flywheel consists of a rotating mass that stores kinetic energy. The internal mounted flywheels allow for enough torque to be produced and transferred, through acceleration and braking, to the hopper's body to perform a hop. In addition they offer the design flexibility for other instruments inclusion. This internal torque produced by the rotating flywheel can be used to change direction or perform a hop with a controlled speed and

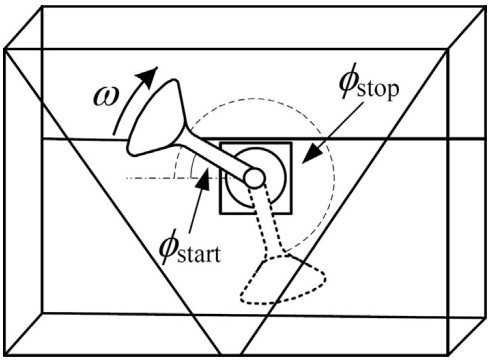


Figure 2.5: MASCOT's mobility mechanism configuration using an eccentric arm [40].

angle. Examples of this torquer hopping approach are the MINERVA rover [39], Hedgehog [18], and the Cubli [31], further detailed in Section 2.2.4.

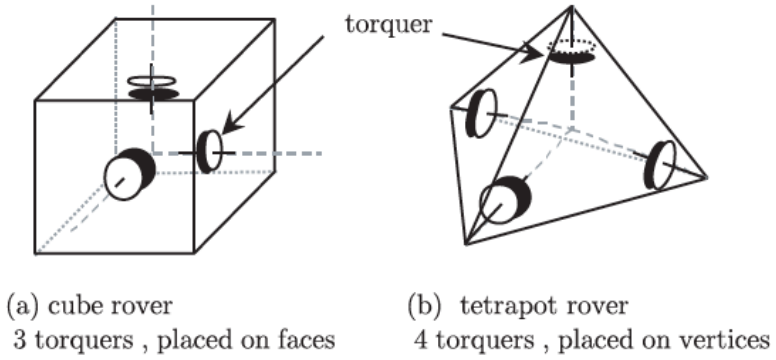


Figure 2.6: 3-DOF actuators in symmetric shape rovers [36].

Different configurations for the torquers placement can be considered. Symmetric designs with three degrees of freedom actuators by three or more *torquers*, displayed in Figure 2.6, allow the hopper to hop in any arbitrary direction regardless of its resting position and attitude, however it also implies more actuators and a heavier rover.

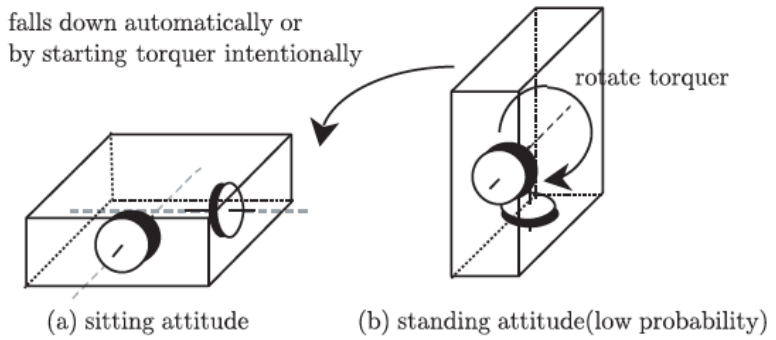


Figure 2.7: 2-DOF actuators in rovers with reduced number of torquers [36].

On the other hand, a configuration as shown in Figure 2.7, with less torquers and only two degree

of freedom actuators, can still move for any attitude, having however to perform a self-righting operation or adjust its orientation if the initial hopper's position is not the required to execute the next hop. The two torquers working in simultaneous can still provide an oblique torque to get out of an undesired stuck position, or to change the hopper's attitude. This configuration leverages a non symmetrical shape and distribution of mass.

### 2.2.4 Literature Review

The main projects and investigation developed on the field of internally-actuated mobility rovers and motion analysis for small-body environment, and that represent the most relevant background for this work, are exhibit in this section. All of them use torquer mechanisms to perform surface mobility through hopping.

#### Cubli

The Cubli is a developed project by the Institute for Dynamic Systems and Control in Switzerland, of a $15cm$ edge cube that can jump up and balance on a corner [31]. The main contribution of this work is the shown ability to hop from a resting position without any external support or mechanism. The Cubli's configuration follows the illustrated Figure 2.6 (a). It has three orthogonal momentum wheels mounted internally on three of its faces, as shown in Figure 2.8. This 3D inverted pendulum system allows for all instruments and actuators to be enclosured in the cube structure.

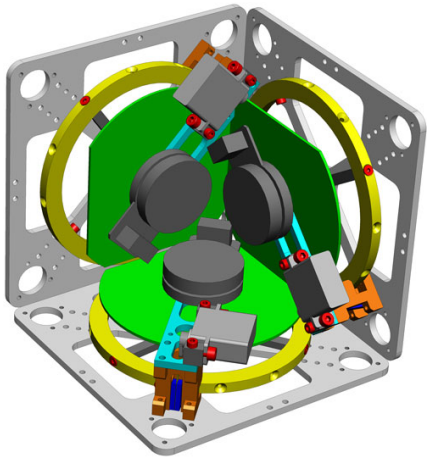

Figure 2.8: Cubli's CAD prototype of the internal mobility system design [31].

To perform a jump, through actuation of the momentum wheels the Cubli can move about one of its edges by abruptly stopping one of its flywheels. It can also balance on its edge by the same principle but with a lower angular velocity prior to the braking, than goes to balancing on a corner by stopping the other two flywheels. The motor torques make sure the platform continues balanced. A detailed explanation of the dynamics and motion of the Cubli can be found in Gajamohan et al. [31].

### MASCOT

The Mobile Asteroid Surface Scout (MASCOT) is a small separate landing package studied and developed by the German Aerospace Center (DLR) [40], for the mission of the Hayabusa-2 spacecraft [15] to the Ryugu asteroid.

The MASCOT lander has a rectangular parallelepiped shape with a total size of $28cm \times 29cm \times 21cm$ and a total mass of approximately $9.8kg$ [17]. All scientific instruments and support elements, including the mobility mechanism, are accommodated inside the rectangular structure. Figure 2.9 shows the MASCOT rover. A complete view on the operations and components of this lander rover, and its successful operation details can be found in [43].

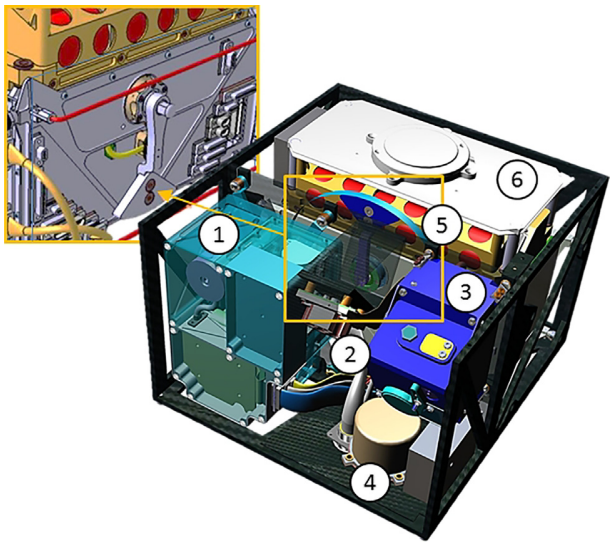


Figure 2.9: MASCOT lander CAD prototype of the internal system design [40]. (1), (2), (3), (4) and (6): Instruments and support elements. (5): Mobility mechanism, shown in top left corner.

The mobility mechanism consists of a small diameter brushless DC motor that accelerates and decelerates an eccentric arm, that is able to rotate with significant revolution. A generated jerk from the stopping of the actuator causes the MASCOT to flip or hop depending on the initial speed of the arm. This rover has no attitude control during the flight motion. The referred eccentric arm mechanism operation is represented in Figure 2.5.

### MINERVA

The MINERVA hoppers, which stands for MIcro/Nano Experimental Robot Vehicle for Asteroids, were developed by the Institute of Space and Astronautical Science (ISAS) from the Japan Aerospace Exploration Agency (JAXA), and were on board of both *Hayabusa* mission to asteroid Itokawa in 2005 [14], and *Hayabusa-2* mission to asteroid 162173 Ryugu in 2018 [16].

Figure 2.10 shows the MINERVA hopper design. MINERVA-I from the first Hayabusa mission assumed a circular base (see Figure 1.3), with the same parameters as MINERVA-II. The parameters of the referred hoppers are listed in Table 2.2. All scientific instruments and mobility mechanism elements are inside the external structure. The external structure has several pins, also referred as spikes, at its

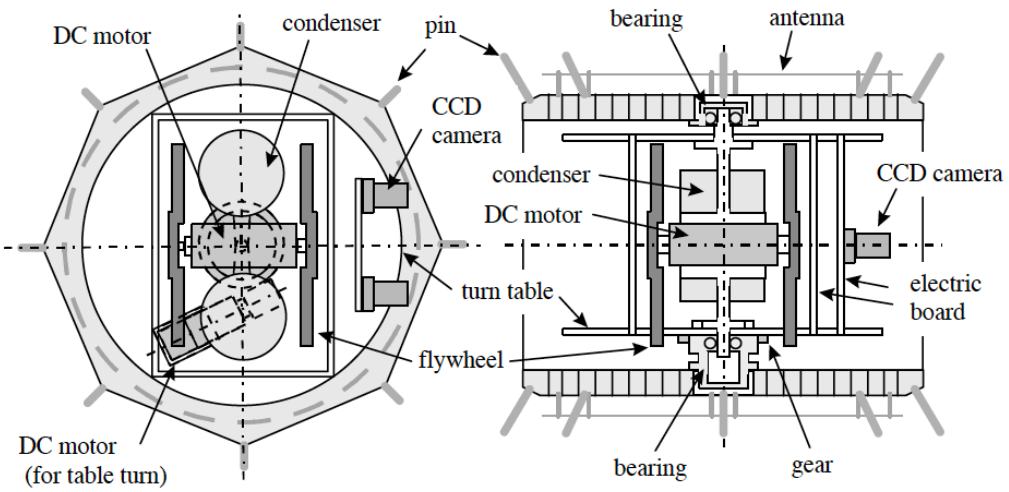


Figure 2.10: MINERVA's design and internal layout [39].

vertices with the purpose to protect the solar panels from the impact against the ground and to increase friction as a hook.

| Parameters | Definition |
|---|---|
| $h = 0.10\ m$ | Hopper's height |
| $d = 0.12\ m$ | Hopper's base diameter |
| $m_r = 5.91\ kg$ | Hopper's total mass |
| $I_r = 1.0 \times 10^{-3}\ kg{\cdot}m^2$ | Hopper's rotational inertia |
| $I_f = 2.3 \times 10^{-5}\ kg{\cdot}m^2$ | Flywheel's rotational inertia |

Table 2.2: MINERVA rover design parameters [14].

The MINERVA rover uses the hopping configuration represented in Figure 2.7, discussed in the previous Section 2.2.3, with two DC motors and flywheels as torquers, and with the particular configuration of Figure 2.11.

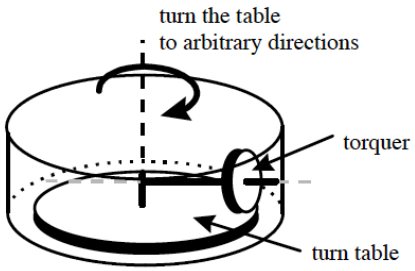


Figure 2.11: Torquer configuration of the MINERVA rover [36].

This concept, composed by a turn table actuated at the bottom face of MINERVA and a orthogonal DC motor attached to flywheels, allows for any directional hop with a two step motion. The "turn table" rotates to the desired direction, and then the orthogonal torquer is actuated with a sufficient torque to

perform a hop about a single-axis [39], as represented in Figure 2.12. The two torquers working in simultaneous can still provide an oblique torque to get out of an undesired stuck position, or to change the hopper's attitude.

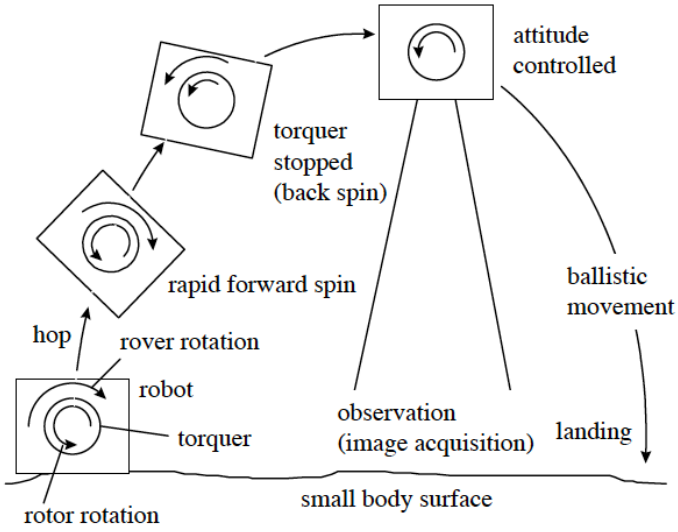


Figure 2.12: Hopping motion of MINERVA rover [39].

MINERVA uses attitude control during the hop flight phase in order to point is instruments for image acquisition, as also illustrated in Figure 2.12.

### Hedgehog

The Hedgehog is a rover hybrid for the exploration of small solar system bodies and was developed by the Department of Aeronautics and Astronautics of Stanford University working alongside with the NASA Jet Propulsion Laboratory (JPL) and the Massachusetts Institute of Technology (MIT). Several advances and studies have been made through out the years to arrive to the current design of the Hedgehog [32, 44–47]. The overview of the referred hopper is going to be taken upon the most recent design [18].

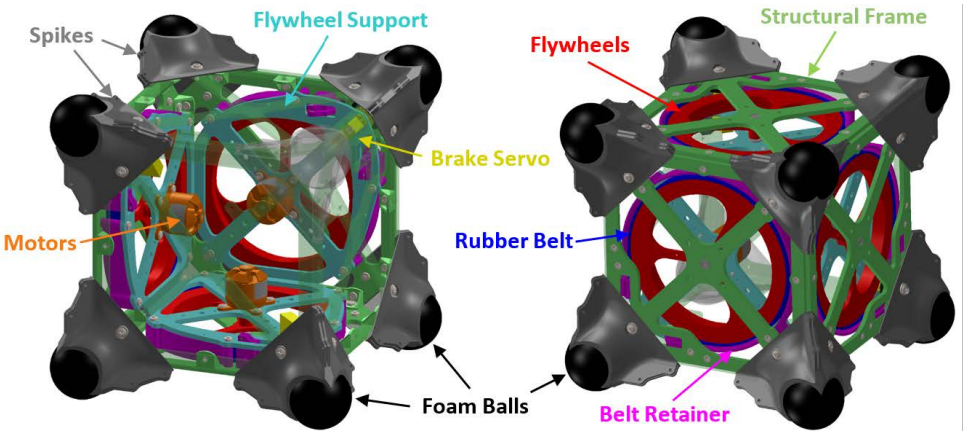


Figure 2.13: Hedgehog prototype and its components [32].

The Hedgehog rover is represented in Figure 2.13 and consists of a $15cm$ edge cube structure with one spike of foam ball tips on each corner. Similar to MINERVA, the spikes provide protection during contact with the surface, and in comparison to the Cubli, indicate the expected contact points for the control mobility and motion planning. The parameters of the Hedgehog are listed in Table 2.3.

| Parameters | Definition |
|---|---|
| $m_r = 2.3\ kg$ | Hopper's total mass |
| $I_r = 0.013\ kg{\cdot}m^2$ | Hopper's rotational inertia |
| $l = 0.168\ m$ | Spikes' length from CG |
| $\alpha = \pi/4\ rad$ | Spike angle |
| $I_f = 9.5 \times 10^{-4}\ kg{\cdot}m^2$ | Flywheel's rotational inertia |
| $g = 5.8 \times 10^{-3}\ m/s^2$ | Phobos' gravity acceleration |

Table 2.3: Hedgehog and environmental mission parameters.

The torquer configuration follows the illustrated Figure 2.6 (a). The platform uses internal actuation to produce reaction torques and generate a hopping motion of the rover, through three mutually-orthogonal flywheels, has shown in Figure 2.13. Each flywheel has $12.7cm$ diameter, rotational inertia of $I_f = 9500g.cm^2$, and a mass of $m_f = 300g$. The flywheels are manipulated by individual DC motors and mechanical band brakes that when applied transfer the flywheel's momentum into torque applied on the hopper, causing it to rotate in an inverted pendulum motion, with a tumbling or hopping motion depending on the initial flywheel speed [32].

### 2.2.5 Main Final Configurations

The most viable determined configuration combines both the Hedgehog and MINERVA principles and approaches. In one hand, the external cubic like shape structure with spikes on its vertices, such as the Hedgehog configuration. On the other hand, the internal configuration of two torquers applied by the MINERVA is favored. This requires for a self-righting maneuver after the hop and subsequent landing rebounds on the ground, but allows for a simpler process of hopping with a two step motion: a twisting maneuver of directional pointing, and then hopping about a axis parallel to the surface. The aforementioned hopping approach is slower but more controllable and accurate than oblique hopping about inclined axes, enabled by the three orthogonal flywheel configuration of the Hedgehog [32]. As referred before, this configuration still provides uncontrolled oblique hops if necessary, to get out of an inconvenient surface region.

DC motors with incorporated flywheels represent the most feasible option as actuators. It allows for all sub-systems to be enclosure in the hopper's structure, it represents a viable space occupation inside the hopper design, with high controllability and flexibility between impulsive transfers and controlled motions for fine tumbling, hopping and instrument pointing. And because it represents a reliable source of power, as previous work and missions showed that such systems can generate the necessary torques and perform controlled hops in emulated microgravity [16, 32].

For the hopping initiation and flywheel actuation, it is favoured the control strategy of slowly spinning

up the flywheels with a motor torque lower than the one that would make the hopper initiate a rotation, so it remains grounded during the actuation of the flywheels. Then a high-torque mechanical brake is applied when the desired flywheel speed is achieved to initiate the hop. This approach was also used and tested by Hockman et al. [32], and provides fast energy transfer if aggressive hops are requested, represents a simple control strategy, and solves any eventual flywheel saturation problems [45]. This control approach will be referred from now on as *build-up strategy*.

It is also leveraged a configuration with attitude control during the flight phase. This provides instrument pointing for picture acquisition like MINERVA, but also the ability to control the hopper's direction and pose for the impact landing, this is further described in sections 3.5.2 and 4.3.

Although, this torquer configuration favours a lower center of mass structure, as a first-order analysis and comprehension of the hopper's motion and dynamics, a uniform distribution of mass will be assumed in the next chapters.

# Chapter 3

# Hopping Dynamics

In this chapter the dynamics involved in the rover's hopping mobility are analyzed and modelled. This analytical work follows the selected configuration and strategy defined in the previous chapter.

Under the configurations described in Section 2.2.5, the rover's hopping movement is performed about a single-axis, controlled by one single flywheel actuation and in which the contact reaction forces with the ground occur about the pair of stance spike tips. This allows a two-dimensional dynamic analysis of the system to describe the single-axis hop executed, in a cut-section perspective as shown in Figure 3.1. The rover's mass distribution is assumed uniform and his centre of mass coincident with its geometric centre. The hopper is modelled in two-dimensions as a disk with equispaced rigid spikes attached, and with a single flywheel driven by a motor at its center of mass, as the commonly used model of passive dynamic walking [48].

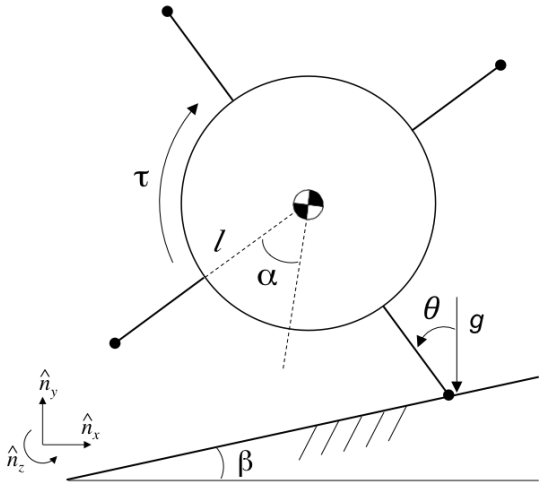


Figure 3.1: Planar representation of the hopper's 2D model.

The angle $\theta$ represents the angle between the stance spike tip and the vertical. The angle $\beta$ is referred to the surface inclination on the hopper's initial position, representing a possible small ramp area existent, or that one of the pair of spikes in contact with the ground is standing in a rock or in higher surface level. For the flight phase and distance covered the remaining surface is considered without inclination.

For a first-order representation of the hopper's motion it is acceptable to assume a flat and homogeneous surface, that collisions with the surface are inelastic and impulsive, and that the stance spike acts as a pin joint and does not slip. These assumptions, despite being unrealistic for small bodies, have been proven to be reliable for first-order estimations and initial analysis of the designs viability, as validated in several previous studies [32, 45, 47] through simulations and experiments. However, the no-slip assumption during the rover's motion does not hold for extreme non-rigid surfaces, such as loose regolith.

Under these assumptions, a conservation of angular momentum approach can be considered and the rover's hopping controlled motion can be divided into a build-up phase, a stride phase, and a flight phase.

1. Build-up phase – occurs with the hopper at rest, due to the *build-up strategy* discussed in Section 2.2.5.
2. Stride phase – occurs before ground contact is lost and while the system is supported by a single spike (or pair of spikes).
3. Flight phase – occurs when there is no longer contact with the surface and the hopper is in a ballistic trajectory.

In the following subsections the phases of motion and the dynamics involved for a single-axis hop performed by the hopper are identified and modelled. Figure 3.2 shows a representation of the three phases.

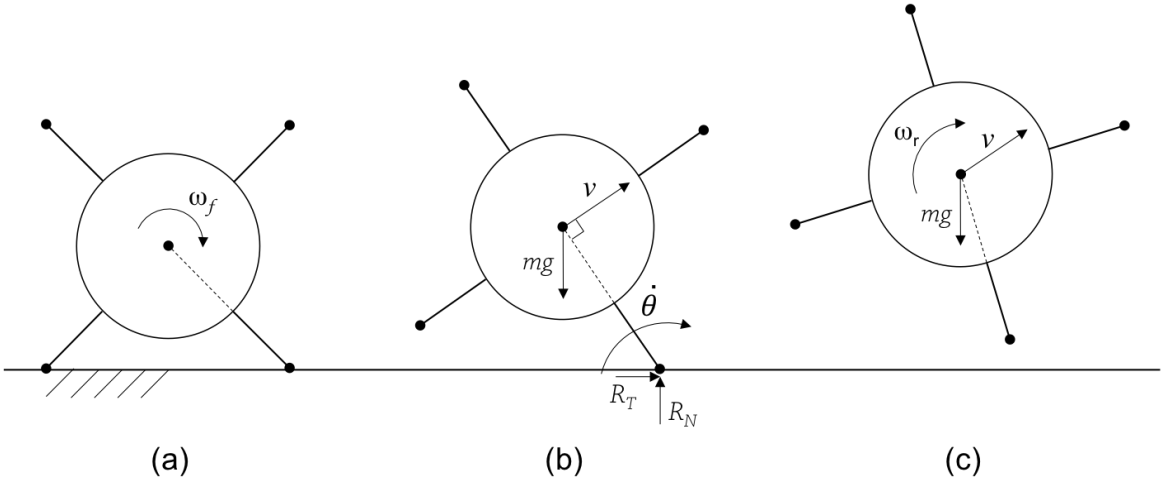


Figure 3.2: Three phases of a single axis hopping motion. Left (a): Build-up phase. Center (b): Stride phase. Right (c): Flight phase.

## 3.1 General Equation of Motion

First, considering that the hopper starts from a resting position on the ground and that a sufficient reaction clockwise torque $\tau$ is generated on the hopper due to the anti-clockwise actuation of the flywheel,

as represented in Figure 3.1, making the rover to rotate in a pivoting motion. In this scenario, to apply a clockwise torque $\tau$ to the hopper an anti-clockwise torque must be present in the flywheel.

Analyzing the stride phase, under the aforementioned assumptions and with special attention to the stance spike acting as a pin joint and does not slip while in contact with the ground, the dynamic model can be described by $\theta$ and $\dot{\theta}$. With $\dot{\theta}$ representing the hopper's angular speed, described by the angle $\theta$ variation through time. In this motion the hopper performs a rotation about its stance spike in a circular motion and does not slip, so the hopper's linear velocity $v = \sqrt{\dot{x}^2 + \dot{y}^2}$ from its centre of mass is then given by $v = l\dot{\theta}$.

Using the Lagrangian mechanics principle for no dissipation,

$$\frac{d}{dt}\frac{\partial L}{\partial \dot{q}} - \frac{\partial L}{\partial q} = \frac{\partial \delta W}{\partial \delta q}, \tag{3.1}$$

with $q = \theta$ and $L = T - V$. The last equation represents the work done by the external forces. For this case in question, and with the hopper at rest on the initial position defined by $(x, y) = (0, l\cos\theta)$, the energy equations can be written as:

$$T = \frac{1}{2}I_r\dot{\theta}^2 + \frac{1}{2}m_r(\dot{x}^2 + \dot{y}^2) = \frac{1}{2}I_r\dot{\theta}^2 + \frac{1}{2}m_r l^2\dot{\theta}^2 \tag{3.2}$$

$$V = m_r g y \tag{3.3}$$

$$y = l\cos\theta \tag{3.4}$$

Hence,

$$L = \frac{1}{2}(I_r + m_r l^2)\dot{\theta}^2 - m_r g l\cos\theta \tag{3.5}$$

$$W = -\tau\theta \tag{3.6}$$

Solving for the Lagrangian equation 3.1:

$$(I_r + m_r l^2)\ddot{\theta} - m_r g l\sin\theta = -\tau \tag{3.7}$$

$$\ddot{\theta}(t) = \frac{m_r g l\sin\theta(t) - \tau}{I_r + m_r l^2} \tag{3.8}$$

The equation of motion is that of an inverted pendulum. And can be also obtained by an angular momentum balance about the stance spike tip from Figure 3.1.

## 3.2 Build-up Phase

This is the first step to perform the desired hopping movement. The rover remains in a stationary position and the flywheels spin up with a torque lower than the one required to make the hopper begin a rotation $\tau < \tau_{max}$, ensuring the hopper remains grounded, until the desired flywheel speed is accomplished. This build-up phase ends with the application of the brake and the consequent momentum transfer from the flywheel to the hopper.

Under this strategy, for the stride phase to be performed in a clockwise motion, the flywheel speed $w_f$ must also be clockwise as shown in Figure 3.2. Considering that the hopper design is symmetric and both spikes on the ground have a length $l$ from their tip to the hopper's center of mass, from Equation 3.8 it is possible to calculated such minimum torque that would make the hopper start the pivoting motion in a clockwise rotation (i.e. $\ddot{\theta} < 0$). By the schematics of Figure 3.1, $\theta(0) = (\alpha+\beta)$, With $\alpha$ representing the spike angle and $\beta$ the surface inclination, and so the maximum allowed torque applied by the flywheel through this strategy is given by:

$$\tau_{max} = m_r g l \sin(\alpha + \beta) \tag{3.9}$$

The torque generated by the flywheel is defined by:

$$\tau = I_f \dot{\omega}_f \tag{3.10}$$

And, since the hopper is in a resting position, the dynamics are described by:

$$\ddot{\theta} = 0 = \dot{\theta} \tag{3.11}$$

This phase ends with the actuation of the mechanical brake and beginning of the stride phase.

## 3.3 Stride Phase

The stride phase initiates with the start of the hopper's movement after the actuation of the flywheel brake. The hopper's center of mass performs a circular motion about its stance spike, while it is in contact with the ground. The flywheel brake can be actuated in different ways and based on two different principles: a high impulsive brake, or a constant braking applied until the flywheel stops. The two distinct approaches involve different dynamics.

### 3.3.1 Instantaneous momentum transfer

In the presence of high friction brakes (e.g. pin brakes or impact hammers), where an impulsive braking is applied, the momentum transfer from the rotating flywheel to the hopper can be assumed instantaneous and without dissipation. With the stride phase beginning immediately after the application of the brake and consequent momentum transfer. For this case, there is no applied torque on the rover

from the flywheel during the stride phase, which results in only one control input variable (i.e. the flywheel speed).

As previously derived, the Equation 3.8 of motion for the stride phase, when no torque from the flywheel is being applied is given by:

$$\ddot{\theta}(t) = \frac{m_r g l \sin\theta(t)}{I_r + m_r l^2} \tag{3.12}$$

The angular momentum of the flywheel prior to the brake is ($I_f \omega_f$) and the angular momentum of the hopper about the stance spike tip immediately after the brake is given by ($I_r \dot{\theta}_0 + l m_r v_0$). Due to the assumption of the spike tip behaving as a pin joint (i.e. no-slip) $v = l\dot{\theta}$. Assuming instantaneous momentum transfer from the flywheel to the rover, by the conservation of angular momentum principle it is obtained:

$$I_f \omega_f = \dot{\theta}_0 (I_r + m_r l^2) \tag{3.13}$$

Resulting in,

$$\dot{\theta}_0 = \frac{I_f \omega_f}{I_r + m_r l^2} \tag{3.14}$$

This represents the angular velocity of the hopper in the instant immediately after the momentum transfer (i.e. in the beginning of the stride phase, $t = 0$). The stride phase begins immediately after the momentum transfer, meaning the hopper's angle $\theta$ in that instant ($t = 0$), from Figure 3.1, is then given by:

$$\theta_0 = \alpha + \beta \tag{3.15}$$

From an energy transfer point of view, initially there is the flywheel kinetic energy just before the brake:

$$E(t^-) = \frac{1}{2} I_f \omega_f^2 \tag{3.16}$$

And immediately after the brake the resulting hopper's kinetic energy:

$$E(t^+) = \frac{1}{2} (I_r + m_r l^2) \dot{\theta}_0^2. \tag{3.17}$$

It is possible to obtain the correspondent energy transfer efficiency from the flywheel to the produced hop after the application of the brake and complete stop of the flywheel, here considered instantaneous:

$$\eta = \frac{E(t^-)}{E(t^+)} = \frac{\frac{1}{2} I_f \omega_f^2}{\frac{1}{2} (I_r + m_r l^2) \dot{\theta}_0^2} \tag{3.18}$$

Using Equation 3.14 it is possible to solve the energy transfer efficiency equation to:

$$\eta = \frac{I_f}{I_r + m_r l^2} \tag{3.19}$$

**Condition to perform a hop**

By analyzing the free body diagram of the system, represented in Figure 3.3, it is possible to identify the transition from stride to flight dynamically (i.e. when the normal force from the surface contact goes to zero), obtaining the required condition for such hopping instant.

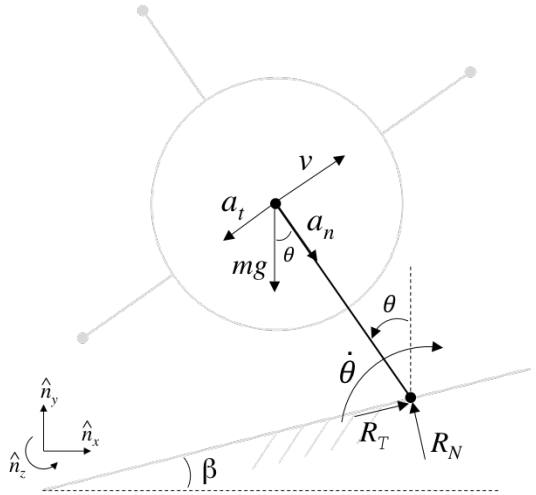


Figure 3.3: Hopper's system free-body diagram schematics for the stride phase for instantaneous momentum transfer.

The hopper is performing a circular motion about the its stance spike, with a radial acceleration $|a_n| = \frac{v^2}{l}$. As no-slip is assumed at the tip of the spike $v = l\omega$, the radial acceleration is given by $|a_n| = l\omega^2$. With $\omega$ representing the rotational speed, $v$ the linear speed in its center of gravity and $l$ the distance between the center of mass and the center of rotation. Considering the figure 3.3 of the problem in study, the centripetal acceleration value is given by $|a_n| = \dot{\theta}^2 l$ and the tangential acceleration value of the hopper given by $|a_t| = \ddot{\theta} l$. As $\theta$ is measured anti-clockwise, the cartesian components of the total linear acceleration of the hopper are given by:

$$\begin{cases} a_x = \dot{\theta}^2 l \sin\theta - \ddot{\theta} l \cos\theta \\ a_y = -\dot{\theta}^2 l \cos\theta - \ddot{\theta} l \sin\theta \end{cases} \tag{3.20}$$

From Figure 3.3, the translation motion equations are written as follow:

$$\begin{cases} R_T \cos\beta - R_N \sin\beta = m_r(\dot{\theta}^2 l \sin\theta - \ddot{\theta} l \cos\theta) \\ R_N \cos\beta + R_T \sin\beta - m_r g = m_r(-\dot{\theta}^2 l \cos\theta - \ddot{\theta} l \sin\theta) \end{cases} \tag{3.21}$$

The first equation of the system (3.21) can be written as:

$$R_T = \frac{m_r(\dot{\theta}^2 l \sin\theta - \ddot{\theta} l \cos\theta) + R_N \sin\beta}{\cos\beta} \tag{3.22}$$

Replacing (3.22) on the second equation of (3.21), results in:

$$R_N \cos\beta + \frac{m_r(\dot{\theta}^2 l \sin\theta - \ddot{\theta} l \cos\theta) + R_N \sin\beta}{\cos\beta} \sin\beta - m_r g = m_r(-\dot{\theta}^2 l \cos\theta - \ddot{\theta} l \sin\theta) \tag{3.23}$$

Multiplying all terms by $\cos\beta$:

$$-m_r g \cos\beta + R_N + m_r l\dot{\theta}^2(\sin\theta\sin\beta + \cos\theta\cos\beta) + m_r l\ddot{\theta}(\sin\theta\cos\beta - \cos\theta\sin\beta) = 0 \tag{3.24}$$

Which can be simplified into:

$$-m_r g \cos\beta + R_N + m_r l\dot{\theta}^2 \cos(\theta - \beta) + m_r l\ddot{\theta} \sin(\theta - \beta) = 0 \tag{3.25}$$

Obtaining finally, from the equation of motion 3.12,

$$-m_r g \cos\beta + R_N + m_r l\dot{\theta}^2 \cos(\theta - \beta) + \frac{m_r g l \sin\theta}{I_r + m_r l^2} m_r l \sin(\theta - \beta) = 0 \tag{3.26}$$

To perform a hop, it is necessary to have loss of ground contact at the stance spike. This will happen at the hopping instant $t_h$, when the normal force $R_N$ crosses from positive to zero marking the end of the stride phase and the beginning of the flight. Considering for the problem in study $-\frac{\pi}{2} < \theta < \frac{\pi}{2} \Rightarrow \cos\theta > 0$. This dynamical required condition ($R_N \leq 0$) can be solved from Equation 3.26 to:

$$\dot{\theta}^2(t_h) > \frac{g\cos\beta}{l\cos(\theta(t_h) - \beta)} - \frac{m_r g l \sin(\theta(t_h))}{I_r + m_r l^2} \tan(\theta(t_h) - \beta) \tag{3.27}$$

With $t_h$ representing the hopping instant.

### 3.3.2 Momentum transfer durative

In the presence of other types of brakes, such as friction disks and band brakes, like the one used and determined as the most effective and reliable by Stanford in the Hedgehog hopper [32], momentum transfer cannot be considered instantaneous. In this braking systems a constant braking torque is assumed $\overline{\tau}$ and applied for a $\Delta t$ time duration of braking until the flywheel comes to a full stop. As shown by Hockman et al. [32], this relation can be written and described by:

$$\overline{\tau}\Delta t = I_f \omega_f \tag{3.28}$$

It is important to study the braking duration $\Delta t$, dependent of the constant torque $\overline{\tau}$ applied, to understand in which period it is inserted in the hopper's motion. It is also important to analyze the effect of the magnitude of the constant torque applied in the hop angle and lateral distance achieved by the hopper.

From Equation 3.28 it is possible to understand the relation between the braking time duration and the input values of the applied braking torque and flywheel angular speed, which will dictate if the flywheel comes to a full-stop before or after the flight phase begins, respectively $\Delta t \leq t_h$ or $\Delta t > t_h$. Being $t_h$ the

hopping instant, transition between stride and flight.

For the same flywheel angular speed, the higher the constant braking torque applied the less amount of time the braking will last ($\overline{\tau} \uparrow \Rightarrow \Delta t \downarrow$). The higher the flywheel speed, the higher the needed braking torque applied to achieve a same braking time ($\omega_f \uparrow \Rightarrow \overline{\tau} \uparrow$).

For a $\Delta t \rightarrow 0$, the impulsive torque applied corresponds to the instantaneous momentum transfer, studied in the previous Section 3.3.1.

To study the cases where $\Delta t$ is finite the equation of motion must be solved. As previously derived for the stride phase the Equation 3.8, for a constant braking system the equation of motion of the hopper is:

$$\ddot{\theta}(t) = \frac{m_r g l \sin\theta(t) - \overline{\tau}}{I_r + m_r l^2} \tag{3.29}$$

If aggressive hops are considered, with high enough torque applied such that it is possible to assume that $\overline{\tau} >> m_r g l \sin\theta$, this means Equation 3.29 can be simplified into a linear second order ordinary differential equation:

$$\ddot{\theta}(t) = \frac{-\overline{\tau}}{I_r + m_r l^2} \tag{3.30}$$

Which allows, through integration, to obtain the analytical expected angular velocity and angle through time, assuming a constant torque.

$$\dot{\theta}(t) = \frac{-\overline{\tau}}{I_r + m_r l^2} t + C_1 \tag{3.31}$$

With $C_1$ representing a real constant value. The initial state is defined by $\dot{\theta}(0) = 0$, hence $C_1 = 0$, resulting in:

$$\dot{\theta}(t) = \frac{-\overline{\tau}}{I_r + m_r l^2} t \tag{3.32}$$

Integrating Equation 3.32, the angle $\theta$ through time can be solved to:

$$\theta(t) = \frac{1}{2} \frac{-\overline{\tau}}{I_r + m_r l^2} t^2 + C_2 \tag{3.33}$$

For a terrain with inclination $\beta$, the initial angle is defined by $\theta(0) = \alpha + \beta$, hence $C_2 = \alpha + \beta$. Which results in:

$$\theta(t) = \frac{1}{2} \frac{-\overline{\tau}}{I_r + m_r l^2} t^2 + \alpha + \beta \tag{3.34}$$

#### Hopping Condition

A similar analysis to the one made in Section 3.3.1 is done to study the stride to flight transition and requirement of the rover to perform a hop, now for a non-instantaneous momentum transfer. The hopper acceleration components are the ones given by Equation 3.20.

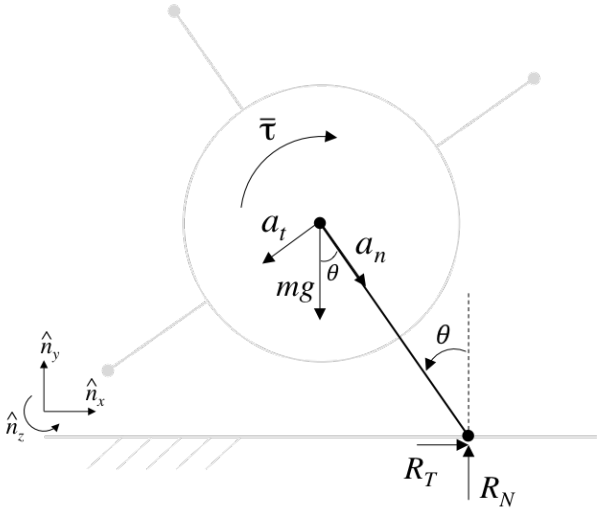


Figure 3.4: Hopper's system free-body diagram for the stride phase when a constant braking torque is being applied, on a level terrain.

For a level terrain as represented in Figure 3.4, the translation motion equations of the hopper's center of mass are:

$$\begin{cases} R_T = m_r(\dot{\theta}^2 l \sin\theta - \ddot{\theta} l \cos\theta) \\ R_N - m_r g = m_r(-\dot{\theta}^2 l \cos\theta - \ddot{\theta} l \sin\theta) \end{cases} \tag{3.35}$$

The equation for the rotational dynamic is given by:

$$\sum M_r = R_T l \cos\theta + R_N l \sin\theta - \overline{\tau} = I_r \ddot{\theta} \tag{3.36}$$

Replacing Equation 3.35 in Equation 3.36:

$$m_r(\dot{\theta}^2 l \sin\theta - \ddot{\theta} l \cos\theta) l \cos\theta + m_r(-\dot{\theta}^2 l \cos\theta - \ddot{\theta} l \sin\theta + g) l \sin\theta - \overline{\tau} = I_r \ddot{\theta} \tag{3.37}$$

Which can be simplified into:

$$-m_r l^2 \ddot{\theta} + m_r g l \sin\theta - \overline{\tau} = I_r \ddot{\theta} \tag{3.38}$$

Obtaining finally:

$$\ddot{\theta} = \frac{m_r g l \sin\theta - \overline{\tau}}{I_r + m_r l^2} \tag{3.39}$$

Which validates the equation of motion previously obtained and defined by Equation 3.29.

Replacing on the second equation of the system of Equations 3.35:

$$R_N - m_r g + m_r \dot{\theta}^2 l \cos\theta + \frac{m_r g l \sin\theta - \overline{\tau}}{I_r + m_r l^2} m_r l \sin\theta = 0 \tag{3.40}$$

To perform a hop, it is necessary to have loss of ground contact at the stance spike. This will happen at the hopping instant $t_h$, when $R_N$ crosses from positive to zero marking the end of the stride phase

and the beginning of the flight. In order to obtain a negative normal force ($R_N < 0$), from Equation 3.40, the required condition can be solved to:

$$R_N = m_r g - m_r \dot{\theta}^2(t_h) l \cos\theta(t_h) - \frac{m_r g l \sin\theta(t_h) - \overline{\tau}}{I_r + m_r l^2} m_r l \sin\theta(t_h) < 0 \tag{3.41}$$

Since for the problem in study $-\frac{\pi}{2} < \theta < \frac{\pi}{2} \Rightarrow \cos\theta > 0$, which allows to write the hopping condition as:

$$\dot{\theta}^2(t_h) > \frac{g}{l\cos\theta(t_h)} - \frac{m_r g l \sin\theta(t_h) - \overline{\tau}}{I_r + m_r l^2} \tan\theta(t_h) \tag{3.42}$$

Considering an inclined surface, with inclination $\beta$, as shown in Figure 3.5, the translation motion equations are the same as in section 3.3.1, represented by Equation 3.21. Equaly solved to the same Equation 3.25. From the equation of motion for the non-instantaneous momentum transfer case, described by Equation 3.29, results finally in:

$$-m_r g\cos\beta + R_N + m_r l\dot{\theta}^2 \cos(\theta - \beta) + \frac{m_r g l \sin\theta(t_h) - \overline{\tau}}{I_r + m_r l^2} m_r l \sin(\theta - \beta) = 0 \tag{3.43}$$

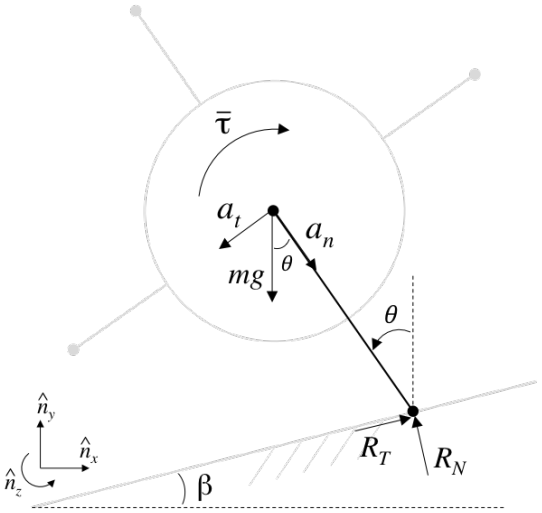


Figure 3.5: Hopper's system free-body diagram for the stride phase when a constant braking torque is being applied, on a terrain with inclination $\beta$.

The condition for the transition from stride to flight, normal force goes to zero, is now written as:

$$\dot{\theta}_h^2 > \frac{g\cos\beta}{l\cos(\theta_h - \beta)} - \frac{m_r g l \sin\theta_h - \overline{\tau}}{I_r + m_r l^2} \tan(\theta_h - \beta) \tag{3.44}$$

For a level terrain (i.e. $\beta = 0$), Equation 3.44 is validated by Equation 3.42.

## 3.4 Flight Phase

The flight phase begins with the loss of surface contact at the stance spike tip. This phase follows a ballistic movement described by the hopping velocity ($\vec{v}_h$) and hopping angle ($\theta_h$), studied in Section 3.3, as well as the hopper's center of mass position at the hopping instant ($x_h$, $y_h$), which all represent the initial conditions of the flight phase motion, as represented in the schematics of Figure 3.6. As stated before, the angle $\beta$ is referred to the surface inclination on the hopper's initial position, for the flight phase and horizontal distance covered analysis the remaining surface is considered without inclination.

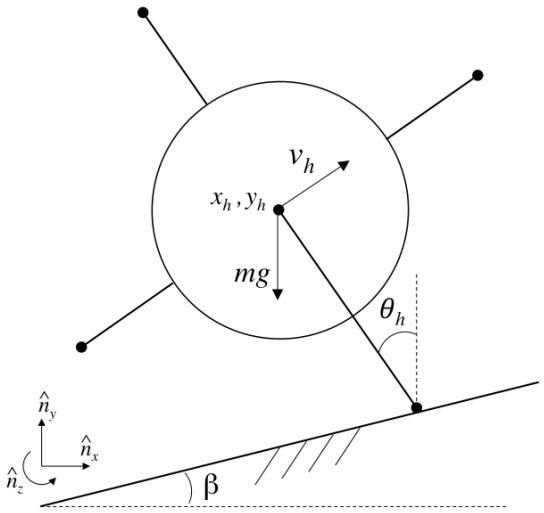


Figure 3.6: Hopper's system schematic diagram for the initial instant of the flight phase.

The magnitude of the velocity at the initial instant of the flight phase is given by:

$$v_{f0} \equiv v_h = l\dot{\theta}_h \tag{3.45}$$

Under a vacuum assumption, the acceleration components of the hopper's motion during the flight phase are:

$$\begin{cases} a_x = 0 \\ a_y = -g \end{cases} \tag{3.46}$$

And so the hopper's velocity components throughout the motion are given by:

$$\begin{cases} v_x = v_h \cos\theta_h \\ v_y = v_h \sin\theta_h - gt_f \end{cases} \tag{3.47}$$

The equations for the displacement are those of the known described 2D ballistic motion:

$$x(t_f) = x_h + v_h t_f \cos\theta_h \tag{3.48}$$

$$y(t_f) = y_h + v_h t_f \sin\theta_h - \frac{1}{2} g t_f^2 \tag{3.49}$$

With $t_f$ representing time during the flight phase (i.e. $t_f = t - t_h$).

From Equation 3.49 when the trajectory's height reaches its initial value (i.e. $y = y_h$), it is possible to obtain the virtual expected time to reach the ground ($t_d$):

$$t_d = \frac{2v_h \sin\theta_h}{g} \tag{3.50}$$

From Equation 3.48 for $t_f = t_d$,

$$x(t_d) - x_n = v_h \frac{2v_h \sin\theta_h}{g} \cos(\theta_h) \tag{3.51}$$

Resulting in the equation for the expected virtual horizontal distance achieve by the hop:

$$d_h = \frac{v_h^2}{g} \sin(2\theta_h), \quad \text{with} \quad v_h = l\dot{\theta}_h \tag{3.52}$$

From Equation 3.47 for $t_f = t_d$, the components of the hopper's virtual expected velocity at the end of the flight phase are given by:

$$\begin{cases} v_e x = v_h \cos\theta_h \\ v_e y = -v_h \sin\theta_h \end{cases} \tag{3.53}$$

During the flight phase the hopper will continue its rotation around itself, with an angular speed of $w_r = \dot{\theta}_h$. The flywheel can also be actuated during the ballistic movement, as previously discussed, for attitude control. This allows to control the hopping direction for instrument pointing, and for the landing and collision with the surface.

## 3.5 Contact Dynamics

In this section the dynamics involved around the contact between the hopper and the ground are studied. Being the small bodies composed by varying morphologies and irregular surfaces, from rocky to fine granular regolith, the contact model is considered to be the most complex to approximate of its reality. Multi-Body-System simulation software [35] or high-fidelity Digital Elevation Models (DEM) [49], can be used to simulate a rover's behaviour on such terrain and surface conditions. For theoretical dynamic approaches, different approximations and assumptions can be considered. The no-slip assumption, which does not hold if the maneuver is performed on non-rigid surfaces (e.g. loose regolith), a flat and homogeneous surface assumption and uniform gravity through the body's surface, which although are not realistic can provide a good first simple approximation with coherent results [32, 47]. A more complex contact model is left for future work.

The contact dynamics are present in different separate stages of the hopper's operation. While the hopper is performing a controlled motion in continuous contact with the surface (i.e. stride phase), and on collisions with the ground upon landing. The two different cases are studied separately, as they represent different dynamic situations and interactions. With the stride phase contact motion modeled

as a *continuous* or *force based* method, and the collisions as an *impulse-momentum* or *discrete* method [50].

### 3.5.1 Contact Motion

In this section the contact motion during the stride phase is modelled. The contact model will be considered as a 2-DoF system composed by a Coulomb friction component that is tangential to the surface, and a spring-damper component that is normal to the surface [51], as shown in Figure 3.7. This model of representing the contact forces was also used in small bodies mobility rover studies of Reid et al. [47] and Hockman et al. [32].

The spring-damper system is composed by an interconnection of a linear spring and a linear damper, representing in parallel respectively the elastic behavior and the dissipation of energy of the contact with the surface. The spring-damper model represents the instability of the contact between the rover and the variable surface. It defines both the potential energy generated by the reaction force on the surface and the dissipative energy due to possible penetration of the hopper's spikes on the loose surface. This contact model is well-suited when dealing with complex nonlinear materials [51].

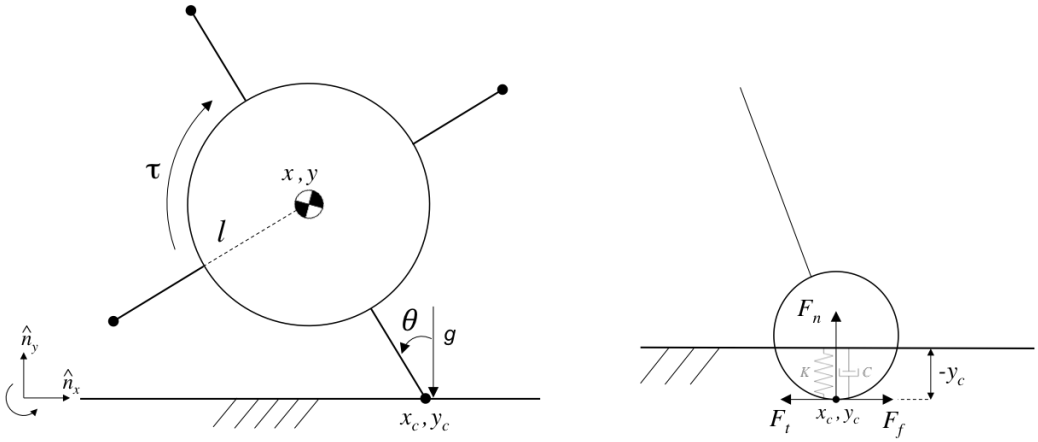


Figure 3.7: Hopper's contact motion dynamics during the stride phase (left), and spike tip contact system schematic (right).

The spike tip point is defined by $(x_c, y_c)$. The centre of gravity position of the hopper is represented by $(x, y)$. The resting initial position of the spike is defined by $(x_c, y_c) = (l \sin(\alpha + \beta), 0)$, and the hopper's initial resting pose is $(x, y, \theta) = (0, l \cos(\alpha + \beta), \alpha + \beta)$.

The contact point during motion is defined by the position of the spike tip relative to the surface, with possible penetration of the surface (i.e. $y_c \leq 0$). With:

$$y = y_c + l \cos\theta \tag{3.54}$$

$$x = l \sin(\alpha + \beta) - l \sin\theta \tag{3.55}$$

$$x_c = x + l \sin\theta \tag{3.56}$$

As a result of the no-slip assumption, $\dot{x}_c = 0$. The normal contact force represented by a spring-damper system is given by:

$$F_n = -Ky_c - C\dot{y}_c \tag{3.57}$$

With $K$ and $C$ representing respectively the surface stiffness and damping parameters. The associated contact potential energy from the spike penetrating $y_c$ into the elastic surface, and the contact dissipative energy from the spike being actively penetrating the surface, are defined as:

$$V_c = \frac{1}{2}Ky_c^2, \quad \text{for } y_c \leq 0 \tag{3.58}$$

$$D_c = \frac{1}{2}C\dot{y_c}^2, \quad \text{for } \dot{y}_c < 0 \tag{3.59}$$

The tangential contact force, represented by the Coulomb friction principle, is given by:

$$\begin{cases} F_t < \mu_s F_n, & \text{if } \vec{v_s} = 0, \\ F_t = \mu_d F_n, & \text{if } \vec{v_s} \neq 0 \end{cases} \tag{3.60}$$

With $\vec{v}_s$ representing the relative velocity between the spike tip and the surface. $\mu_s$ and $\mu_d$ are the static and dynamic friction coefficients, respectively. Due to the no-slip assumption, for the stride phase the first equation of the system of Equations 3.60 is applicable.

The contact dynamics are now modelled using the Lagrangian approach:

$$\frac{d}{dt}\frac{\partial T}{\partial \dot{q}} - \frac{\partial T}{\partial q} + \frac{\partial D}{\partial \dot{q}} + \frac{\partial V}{\partial q} = \frac{\partial \delta W}{\partial \delta q} \tag{3.61}$$

With each term defined bellow accordingly, and its definition displayed in Table 3.1:

$$T = \frac{1}{2}m_r(\dot{x}^2 + \dot{y}^2) + \frac{1}{2}I_r\dot{\theta}^2 \tag{3.62}$$

$$V = m_r g y + V_c \tag{3.63}$$

$$D = D_c \tag{3.64}$$

$$W = -\tau\theta + W_c \tag{3.65}$$

| Term | Definition |
|---|---|
| $T$ | Kinetic energy |
| $D$ | Dissipative energy |
| $D_c$ | Dissipative energy due to contact |
| $V$ | Potential energy |
| $V_c$ | Potential energy due to contact |
| $W$ | Virtual work of external forces |
| $W_c$ | Work against friction |

Table 3.1: Terms definition of the Lagrange equation.

The virtual work done against friction $W_c = F_f x_c$, with $F_f = -sign(\dot{x_c})\mu_d F_n$, is disregarded under the no-slip assumption.

The derivatives of Equations 3.54 and 3.55 are:

$$\begin{cases} \dot{y} = \dot{y_c} - l\dot{\theta}\sin\theta \\ \dot{x} = -l\dot{\theta}\sin\theta \end{cases} \tag{3.66}$$

Replacing Equations 3.54 and 3.66 on the system energy equations from Equation 3.62 to 3.64, it is obtained:

$$\begin{aligned} T &= \frac{1}{2}m_r(l^2\dot{\theta}^2\cos^2\theta + l^2\dot{\theta}^2\sin^2\theta - 2\dot{y_c}l\dot{\theta}\sin\theta + \dot{y_c}^2) + \frac{1}{2}I_r\dot{\theta}^2 = \\ &= \frac{1}{2}m_r(l^2\dot{\theta}^2 - 2\dot{y_c}l\dot{\theta}\sin\theta + \dot{y_c}^2) + \frac{1}{2}I_r\dot{\theta}^2 \end{aligned} \tag{3.67}$$

$$V = m_r g(l\cos\theta + y_c) + \frac{1}{2}Ky_c^2 \tag{3.68}$$

$$D = \frac{1}{2}C\dot{y_c}^2 \tag{3.69}$$

$$W = -\tau\theta \tag{3.70}$$

Which allows to solve Equation 3.61 into the two degree of freedom $q = (y_c, \theta)$ system, with $y_c \leq 0$.

$$\frac{\partial T}{\partial \dot{y_c}} = m_r(-\dot{\theta}l\sin\theta + \dot{y_c}) \tag{3.71}$$

$$\frac{d}{dt}\left(\frac{\partial T}{\partial \dot{y_c}}\right) = m_r(\ddot{y_c} - \ddot{\theta}l\sin\theta - \dot{\theta}^2 l\cos\theta) \tag{3.72}$$

$$\frac{\partial T}{\partial y_c} = 0 \tag{3.73}$$

$$\frac{\partial V}{\partial y_c} = m_r g + Ky_c \tag{3.74}$$

$$\frac{\partial D}{\partial \dot{y_c}} = C\dot{y_c} \tag{3.75}$$

$$\frac{\partial T}{\partial \dot{\theta}} = m_r(l^2\dot{\theta} - \dot{y_c}l\sin\theta) + I_r\dot{\theta} \tag{3.76}$$

$$\frac{d}{dt}\left(\frac{\partial T}{\partial \dot{\theta}}\right) = m_r(l^2\ddot{\theta} - \ddot{y_c}l\sin\theta - \dot{y_c}l\dot{\theta}\cos\theta) + I_r\ddot{\theta} \tag{3.77}$$

$$\frac{\partial T}{\partial \theta} = -m_r\dot{y_c}l\dot{\theta}\cos\theta \tag{3.78}$$

$$\frac{\partial V}{\partial \theta} = -m_r g l \sin\theta \tag{3.79}$$

$$\frac{\partial D}{\partial \dot{\theta}} = 0 \tag{3.80}$$

$$\frac{\partial W}{\partial \theta} = -\tau \tag{3.81}$$

Obtaining finally from Equation 3.61, the resulting system of equations that govern this motion:

$$\begin{cases} m_r(\ddot{y}_c - \ddot{\theta} l \sin\theta - \dot{\theta}^2 l \cos\theta) + C\dot{y}_c + K y_c + m_r g = 0 \\ (m_r l^2 + I_r)\ddot{\theta} - \ddot{y}_c m_r l \sin\theta - m_r g l \sin\theta = -\tau \end{cases} \tag{3.82}$$

### 3.5.2 Landing

Here the impact model is developed to describe the first collision between the hopper and the ground upon landing.

The landing envelope is composed by the rover's first collision with the ground after a hop and the following bounces until the hopper comes to a rest position. The landing envelope has been described by authors as stochastic [52]. Mainly due to the highly sensitive to spin and orientation subsequent trajectories, and the unpredictable bouncing that follows the first impact due to the surface properties, as shown in Hockman and Pavone [52] and Li et al. [53].

Although for the purpose of this rovers' operation stopping in a specific point is not crucial, the precision of the final landing area is quite important to avoid additional necessary tumbling motions to arrive to the desired area. The soft landing and rebound prevention as been a challenge to mobile hoppers throughout the years and still represents one of the biggest obstacles to overcome. Several mechanisms were studied and proposed [46, 54, 55], but a simple and reliable mechanism is yet to be created.

Understanding the stochastic process surrounding the landing phase, the analysis in this work is focused on the dynamics present on the first impact of the hopper on the surface. When the explored body characteristics and surface map are well known, it is possible to model its surface and study the expected landing and rest positions of the rover, after performing a hop, through simulation software and a stochastic motion planing [52]. Here, for simplification purposes in a first-order analysis, the surface is assumed perfectly flat.

The hopper configuration used is the same as stated before in Section 2.2.5. In this scenario, the eight spike tips represent the possible contact points of impact between the hopper and the surface. Three possible impact configurations are considered depending on the number of spikes that collide with the surface: one spike impact, simultaneous impact of two spikes from the same edge, or impact of one facet of four spikes.

Here the impact dynamics at one contact point will be studied in order to better comprehend the

importance of the several parameters and to analyze the energetic and kinetic relations from the impact. The representation of the impact geometry is illustrated in Figure 3.8.

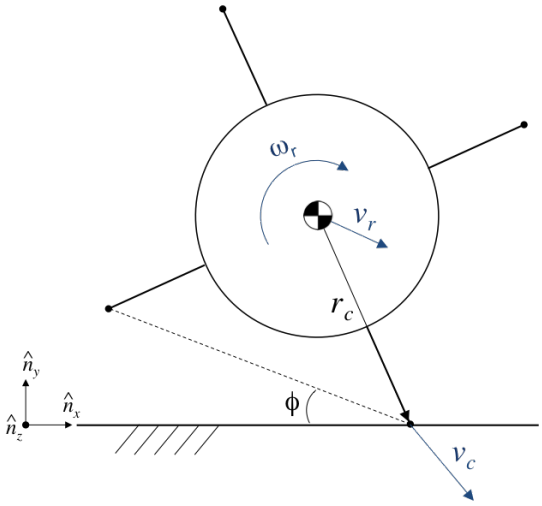


Figure 3.8: Schematics of the hopper's impact on the surface.

**Impact Model**

To model the considered inelastic frictional impact problem it is assumed that collision occurs during an infinitesimally short amount of time and that the net impact force, $\boldsymbol{F_c}$, applied at the contact point, is significantly larger than the gravitational force, allowing this last to be neglected. The impact force acting at the contact point during the collision exerts an impulse, $\boldsymbol{P}$, on the hopper. The position and attitude of the hopper are considered to remain unchanged for the duration of the impact.

The impact is composed by a compression phase, in which the bodies compress against each other while the relative normal velocity is reduced and the corresponding energy stored internally as mechanical energy. And a restitution phase, during which part of the stored energy returns to the bodies with a possible positive relative velocity. The two phases are related accordingly with the Stronge's energetic hypothesis [56] displayed in Equation 3.83, best applicable for this type of eccentric collisions [57].

$$e^2 = \frac{E_r}{E_c} \tag{3.83}$$

Where $0 \leq e \leq 1$ is the coefficient of restitution, and $E_c$ and $E_r$ are respectively the energy absorbed during compression and the released energy during restitution.

The hopper's contact point net velocity, relative to the surface body, $\boldsymbol{v_c}$, is given by:

$$\boldsymbol{v_c^-} = \boldsymbol{v_r^-} + \boldsymbol{\omega_r^-} \times \boldsymbol{r_c} \tag{3.84}$$

In which $\boldsymbol{\omega_r}$ and $\boldsymbol{v_r}$ are respectively the hopper's angular and linear velocity at its center of mass, and $\boldsymbol{r_c}$ the position vector of the contact point, as illustrated in figure 3.8. For each quantity the superscripts '-' and '+' represent, respectively, its value just before and after the impact. The highlighted in bold

variables indicate a vector with referential coordinates.

Considering the aforementioned assumptions, the hopper translational and rotational dynamics during the impact process are written as:

$$\dot{\boldsymbol{v}}_r = \frac{\boldsymbol{F}_c}{m_r} \tag{3.85}$$

$$\boldsymbol{I}_r \dot{\boldsymbol{\omega}}_r = \boldsymbol{r}_c \times \boldsymbol{F}_c \tag{3.86}$$

Leading to the following expressions for the change of translational and rotational velocity from the impact:

$$\Delta \boldsymbol{v} = \frac{\boldsymbol{P}}{m_r} \tag{3.87}$$

$$\Delta \boldsymbol{\omega} = \boldsymbol{I}_r^{-1}(\boldsymbol{r}_c \times \boldsymbol{P}) \tag{3.88}$$

Which results in the post-impact hopper's velocity and angular velocity:

$$\boldsymbol{v}_r^+ = \boldsymbol{v}_r^- + \Delta \boldsymbol{v} \tag{3.89}$$

$$\boldsymbol{\omega}_r^+ = \boldsymbol{\omega}_r^- + \Delta \boldsymbol{\omega} \tag{3.90}$$

As aforementioned, the hopper's angular velocity and attitude, more precisely the impact inclination angle $\phi$, have a significant effect on the velocity after impact, and consequently on the following rebounds. Based on that, the attitude control strategy during the flight phase constitutes an important advantage for the landing performance, allowing a controllable directional approach. Landing on a pair of spikes or on a full facet of four spikes are the two approaches that provide shorten landing distance [53].

Without a landing mechanism it is difficult to obtain a soft landing with the hopper. In Li et al. [53] several impact configurations for different surface properties were studied. The single edge impact (representing the pair of spikes impact in this work), with impact attitude and angular velocity control can change the post-impact velocity to favor a convenient landing path, shortening the distance between the first impact and the final resting position of the hopper. The referred study showed that such strategy improved significantly the landing distance in comparison to the other type of landing, specially to uncontrolled landing, for both flat and uneven terrain. However, the rebound distance still represents between $15 - 20\%$ of its hopping distance [53]. This suggests that, alongside that approach, the application of a simple landing mechanism would improve the landing by reducing the post-impact velocity magnitude.

For the purpose of the operation and mission of such rovers, landing on a specific point is not important, but rather a determined area. The aim is to improve the precision of the hopper's resting position after a hop, by reducing the number and strength of the hopper's resultant bounces that follow the first impact with the surface. Hence, the resulting proposed configuration and concept (see Section 4.3.2) relate with an energy dissipation principle, such that a significant part of the absorbed energy during the compression phase of the impact is in the form of dissipative energy by a damping mechanism on the contact points (i.e. the spikes). Which will produce a lower resultant velocity after the first impact in comparison to the rigid spikes in the Hedgehog design. This new proposed configuration is further

detailed in Section 4.3. The impulse model and landing simulations are left for future work, considering it is more interesting its simulation through a complex surface modelling software.

# Chapter 4

# Numerical Simulations and Results

The previous sections described the methods and analysis for modelling the hopper's motion and small-body environment. In order to solve the system of equations and conditions that govern the hopper's motion and interaction with the surface, numerical simulations were performed.

The simulations were performed and programmed using the software MATLAB, and a *ode45* function for the numerical integration, which corresponds to a fifth-order Runge-Kutta integrator. Throughout this chapter the numerical implementation and the simulation results are presented and discussed.

## 4.1 Numerical Model

The numerical integration of the equations of motion is performed using a fifth-order Runge-Kutta integrator method [58]. This method is a complex Euler-Step propagation, which approximates the state $\boldsymbol{Y_1}$ at some time $t_1 = t_0 + h$ from the initial state $\boldsymbol{Y_0}$ at $t_0$, where $h$ is the step size. The generic step propagation can be defined as:

$$Y_{n+1} = Y(t_n + h) = Y_n + h\dot{Y}_n \approx Y_n + h \cdot \sum_{i=1}^{p} b_i k_i \tag{4.1}$$

Where $k_i$ are calculations of the equations of motion $\dot{\boldsymbol{Y}}$ at certain instants $t$ and variable states $\boldsymbol{Y}$:

$$k_i = \dot{Y}(t_n + h \cdot c_i, Y_n + h \cdot \sum_{j=1}^{i-1} a_{ij} k_j) \tag{4.2}$$

In which $b_i$, $c_i$ and $a_{ij}$ are coefficients of the integration method. This propagation method uses a fourth-order secondary method to evaluate the accuracy of the integration, and select the proper step size $h$. A relative tolerance for this evaluation was defined at $\epsilon = 10^{-12}$. Considering that the numerical integration is only required for the stride phase of motion, the event check that stops the integration is defined by the hopping condition of loss of ground contact.

Soil and surface's physical parameters of asteroids and comets are not fully known, and are often extremely disparate. The values used for the simulations are only representative from the data available [20], and from previous missions information. The following surface parameters were used for the

simulations performed in this section: surface stiffness $K = 10000\ [N/m]$, surface damping $C = 1000\ [Ns/m]$.

## 4.2 Results and Discussion

The numerical model is performed to the stride phase, considering the build-up phase and flight phase follow an explicit motion as described in Sections 3.2 and 3.4. Several simulations were performed to study the different scenarios, with the important results and data presented.

### 4.2.1 Instantaneous momentum transfer brake

Here the simulations for the case of the instantaneous momentum transfer from the flywheel to the hopper are performed, in which no torque is being applied during the stride phase motion (see section 3.3.1). The control input variable in this case is only the flywheel speed prior to the braking.

The initial states for the equations of motion determined by Equation 3.82, with $\tau = 0$, are described as:

$$Y = \begin{bmatrix} y_c \\ \theta \\ \dot{y_c} \\ \dot{\theta} \end{bmatrix} \quad Y_0 = \begin{bmatrix} -0.0001 \\ \alpha + \beta \\ 0 \\ \frac{I_f \omega_f}{I_r + m_r l^2} \end{bmatrix} \tag{4.3}$$

The simulation results, represented in Figure 4.1, show that for an high impulsive brake with an instantaneous momentum transfer scenario, it is safe to assume that the stride phase duration is zero for any flywheel initial speed. And that the flight phase initiates immediately after the momentum transfer. This results in $t_h \equiv t_0$, hence the correspondent hopping angle and hopping angular speed are given by:

$$\theta_h = \alpha + \beta, \qquad \dot{\theta}_h = \frac{I_f \omega_f}{I_r + m_r l^2} \tag{4.4}$$

From the known performed ballistic trajectory of the hopper during flight (see Section 3.4), and using the concluded expressions of Equation 4.4, it is possible to write the flywheel's initial rotational speed $\omega_f$ as function of a desired hopping distance:

$$\omega_f(d_h) = \sqrt{\frac{d_h g}{\eta^2 l^2 \sin(2(\alpha + \beta))}} \tag{4.5}$$

In this regime, Equation 4.4 demonstrates that the hopping angle is determined solely by the spike geometry and the surface inclination. From Equation 3.52, provided by the ballistic flight trajectory, the lateral distance is maximized by a hopping angle of 45°. Facing different surfaces inclinations through the hopper's mobility operations, this optimised angle can only be achieve or approached in all occasions with a spike configuration of variable angle ($\alpha$). Also, when facing larger obstacles a higher hopping angle is desired in order to perform stiffer hops. The variable angle spike configuration (i.e. adjustable

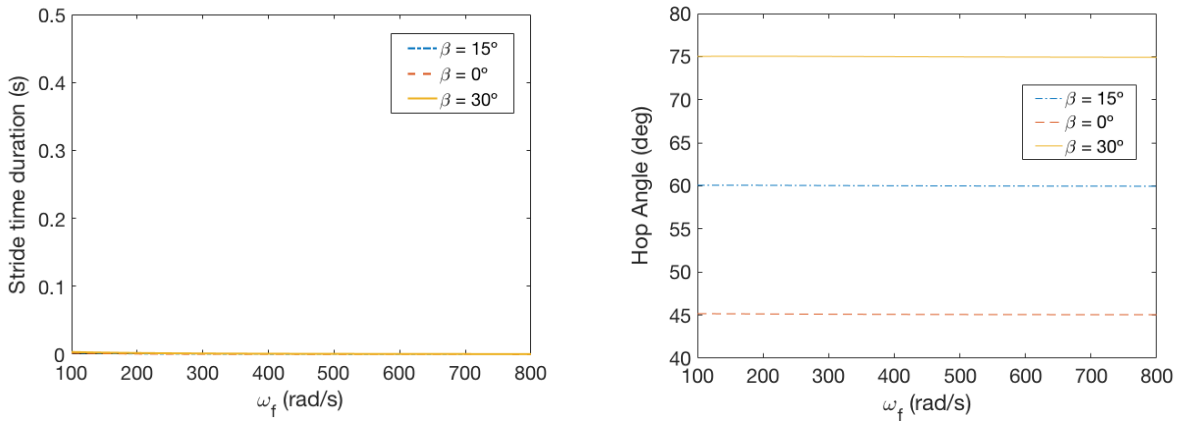


(a) Stride duration

(b) Hop Angle

Figure 4.1: Instantaneous momentum transfer brake results, for the parameters listed in Table 2.3 and three different surface inclination angle. (a): Duration of the stride phase in terms of the flywheel speed. (b): Hop angle as function of the flywheel speed.

$\alpha$) allows for, in an instantaneous momentum transfer, to control the hopping angle ($\theta_h$) depending of the surrounded conditions and ground characteristic, as further detailed in Section 4.3.

### 4.2.2 Influence of Gravity

In the previous Section 4.2.1, it was established that for an instantaneous momentum transfer from the flywheel to the hopper, the hopping would start immediately, with the stride phase being also instantaneous and its duration zero. Using the resultant Equation 4.5, it is possible to analyze the relation existent between the necessary flywheel initial angular speed $w_f$ and the gravitational acceleration $g$ of the explored body, to perform a hop with a desired horizontal distance $d_h$. The usual mission's profile of the studied hopper require considerable transverse with long distance hops. Figure 4.2 exhibits the plot for a $50m$ horizontal hop, under the aforementioned scenario and with the design parameters of the Hedgehog, listed in Table 2.3. In Table 4.1 are listed the results of the required flywheel values of the aforementioned plot for reference bodies.

| Target body | $w_f$ $(rad/s)$ |
|---|---|
| Earth | $1.5 \times 10^4$ |
| Moon | $6152$ |
| Phobos | $382$ |
| Asteroid Ryugu | $63$ |

Table 4.1: Required approximate flywheel speed to achieve a 50m hop horizontal distance, in reference target Celestial Bodies. Using the Hedgehog parameters listed in Table 2.3.

It is visible that the required flywheel initial angular speed behaves exponentially as function of the gravitational acceleration of the explored body. This shows the high dependence to gravity in order to perform a hop. The results support that the presented hopper's mobility is only viable for low-gravity bodies. As Figure 4.2 demonstrates, for a hopper with the Hedgehog design, the feasible flywheel speed generated is only viable for gravity levels of $10^{-5}$ to $10^{-2}$ $m/s^2$ [32].

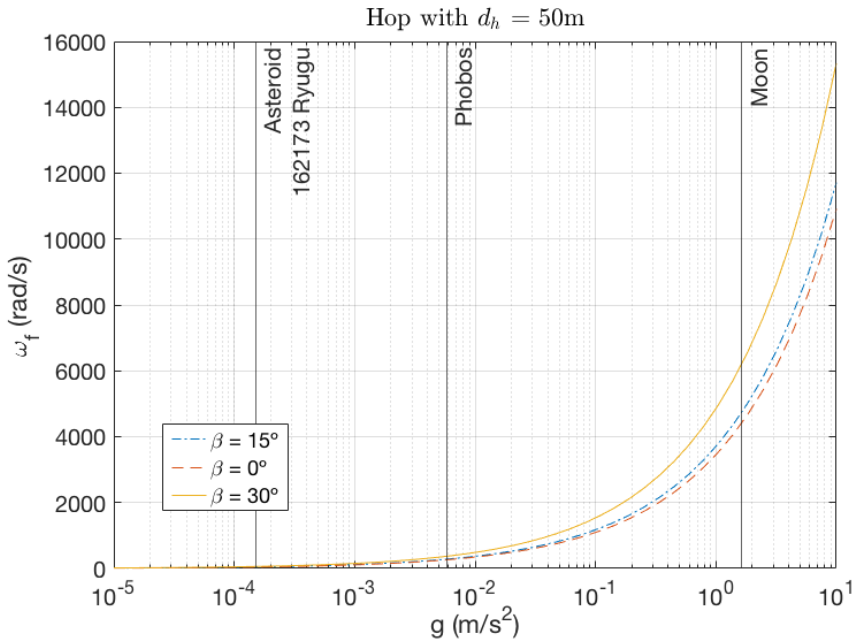


Figure 4.2: Required flywheel speed as function of the gravitational acceleration, to achieve a 50m hop horizontal distance. Using the Hedgehog parameters listed in Table 2.3.

### 4.2.3 Constant torque braking

In this section, are presented the simulations for the case in which the momentum transfer from the flywheel to the hopper is not instantaneous, and a constant brake ($\bar{\tau}$) is being applied until the flywheel comes to a complete stop (see Section 3.3.2).

The initial state for the equations of motion determined by Equation 3.82, is defined by:

$$Y = \begin{bmatrix} y_c \\ \theta \\ \dot{y_c} \\ \dot{\theta} \end{bmatrix} \quad Y_0 = \begin{bmatrix} -0.0001 \\ \alpha + \beta \\ 0 \\ 0 \end{bmatrix} \tag{4.6}$$

The results of the simulations are plotted in Figures 4.3, 4.4, and 4.5, for the Hedgehog parameters (see Table 2.3) and a flywheel initial speed of $2000rpm$ ($209.44rad/s$). And in Figures 4.6, 4.7, and 4.8, for a flywheel initial speed of $5000rpm$ ($523.6rad/s$).

First, comparing the two situations, the low influence of the flywheel angular speed on the stride phase duration and hop angle, as well as the high influence on the hop distance travelled, are shown and in agreement with the analytical model. The constant braking torque applied to the flywheel has significant influence in all. The results for the stride phase duration in terms of the applied braking torque are in agreement with the expected relation from the dynamical analysis of section 3.3.2. Decreasing for an increase of the torque, and tending to zero for high torque values. The high torque results for both the hop distance and hop angle are also in agreement with the calculated relations of the dynamic analysis.

The inflection point on the curves where there is a change of behaviour marks the constant torque

value $\overline{\tau}$ from which the flywheel is fully stopped before the stride phase comes to an end. Prior to that torque value, the flight phase is initiated before the flywheel comes to a complete stop. Torque brakes above that point are favored, considering it not only simplifies the actuation input for the hop to the flywheel speed prior to the brake, but also allows for all the momentum generated on the flywheel during the build-up phase to be used for the hop.

From Figures 4.5 and 4.8, it is visible that after the aforementioned changing point, when in the presence of surface inclination $\beta$, the hopping distance achieved decreases until it starts converging for higher torque values. This is a result of the hopping angle deviation from its desired value of $45°$, which does not happen in the case where there is no surface inclination (i.e. $\beta = 0°$), as shown in Figures 4.4 and 4.7. This can be solved by the implementation of an angle adjusting mechanism on the spikes, actuated when the hopper is standing with inclination. Figure 4.10 shows the resultant changes in the hop distance when adjusting the spike angle to $30°$ instead of the $45°$ fixed angle used in the Hedgehog. In the presence of surface inclination, for both $\beta = 15°$ and $\beta = 30°$, it shows clear improvement on the hop distance obtained for higher torque brake values, comparing with the results of Figure 4.8. For the surface inclination of $\beta = 15°$, the hop distance achieved by the adjusted spike angle to $\alpha = 30°$ is improved between 30% to 45%, for high torque values between 6 and 100 Nm. As also supported by Figure 4.9, where for a spike angle of $30°$ and surface inclination of $15°$, the hop angle for higher torques is closer to the $45°$ for maximized hopping distance. These results represent evidences of the interest of studying the implementation of spikes that variate their angle, and consequently adjust and adapt to different surface inclination and conditions.

From Figure 4.10, it is also noticeable that when applying a $30°$ spike angle in a leveled surface (i.e. $\beta = 0°$), the hop distance for high torques changes in comparison to the $45°$ spike configuration. The required torque values to achieve the same hop distance are higher, identically to the cases with surface inclination, but it also is able to converge to a longer hop distance for higher torques. This is possibly explained by the surface characteristics of the damping and stiffness coefficient values used by the contact model, which in this case may favored a $30°$ spike angle. The distance covered for high torques is not affected, however, this spike angle adjustment has influence on the hop angle of the leveled surface case, which results in a lower ballistic trajectory that in reality might encounter surface obstacles. In conclusion, the spike angle variation must be only considered to the situations with surface inclination.

Several cases were simulated with different spike's length. In Figure 4.11, it is plotted the case of a length from spike tip to the hopper's center of mass of $l = 22.6cm$. It was visible in all cases simulated that longer spikes achieved smaller horizontal hop distances, as demonstrated by comparing Figure 4.8 of a $l = 16.8cm$, with Figure 4.11 of a $l = 22.6cm$. This result is in agreement with the hop efficiency relation to the length of spikes, as previously described by 3.19. And it supports the configuration of shorter spikes.

Even though, the surface constants are not the same and the approach used in Hockman et al. [32] leverages a momentum conservation principle rather than the Lagrange energetic principle used in this work, and as used in [47], the curves from the resulted simulations behave accordingly with the results

obtained in Hockman et al. [32].

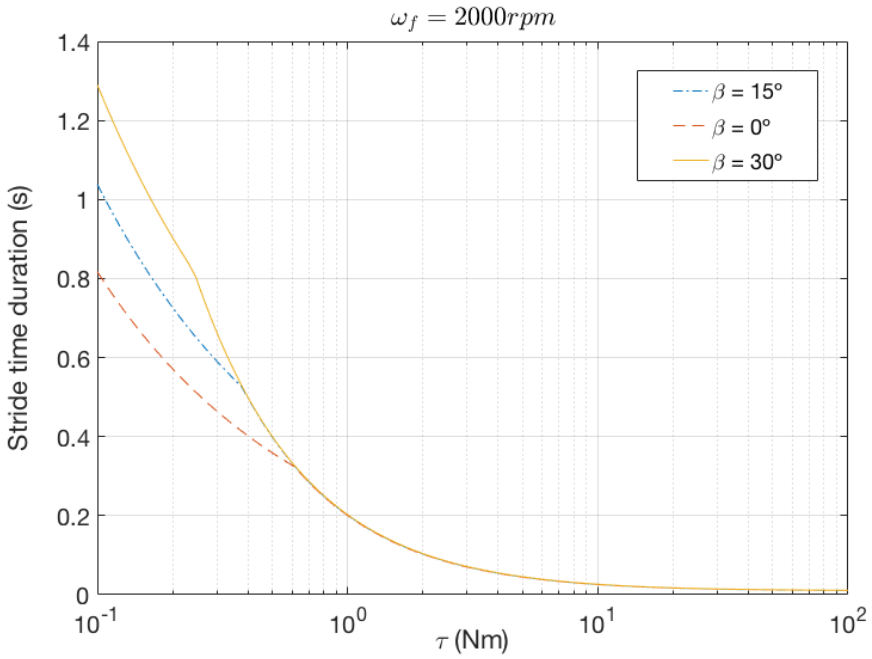


Figure 4.3: Duration of the stride phase in terms of the applied braking torque, for an initial flywheel speed of $\omega_f = 2000rpm$ and the parameters listed in Table 2.3.

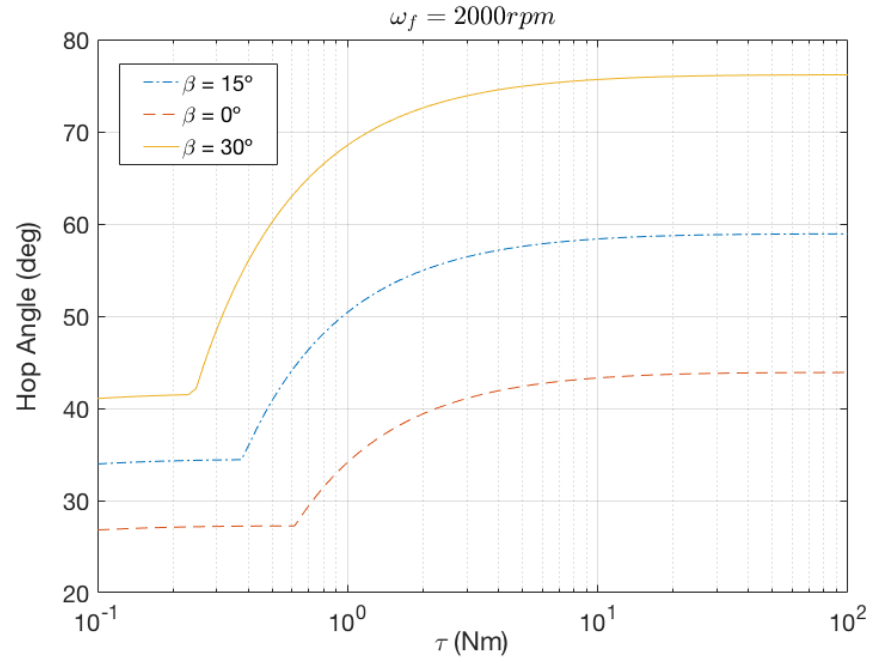


Figure 4.4: Hop angle achieved at the end of the stride phase in terms of the applied braking torque, for an initial flywheel speed of $\omega_f = 2000rpm$ and the parameters listed in Table 2.3.

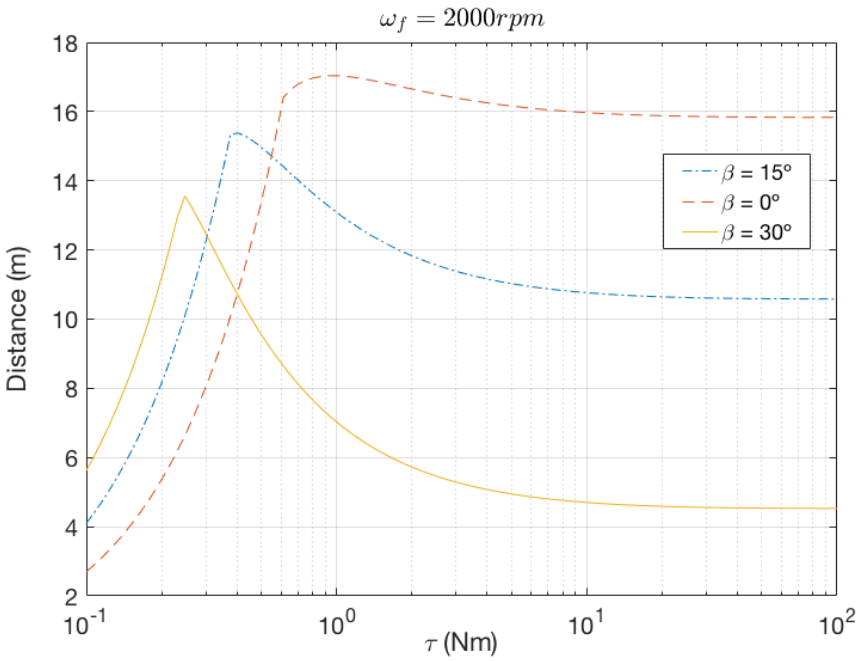


Figure 4.5: Horizontal hop distance achieve by the hopper in terms of the applied braking torque, for a initial flywheel speed of $\omega_f = 2000rpm$ and the parameters listed in Table 2.3.

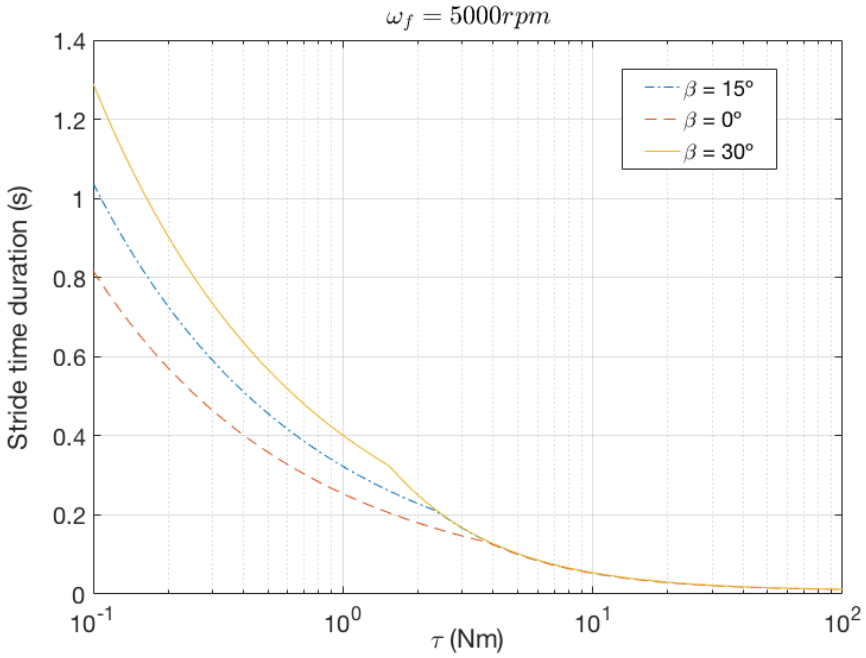


Figure 4.6: Duration of the stride phase in terms of the applied braking torque, for an initial flywheel speed of $\omega_f = 5000rpm$ and the parameters listed in Table 2.3.

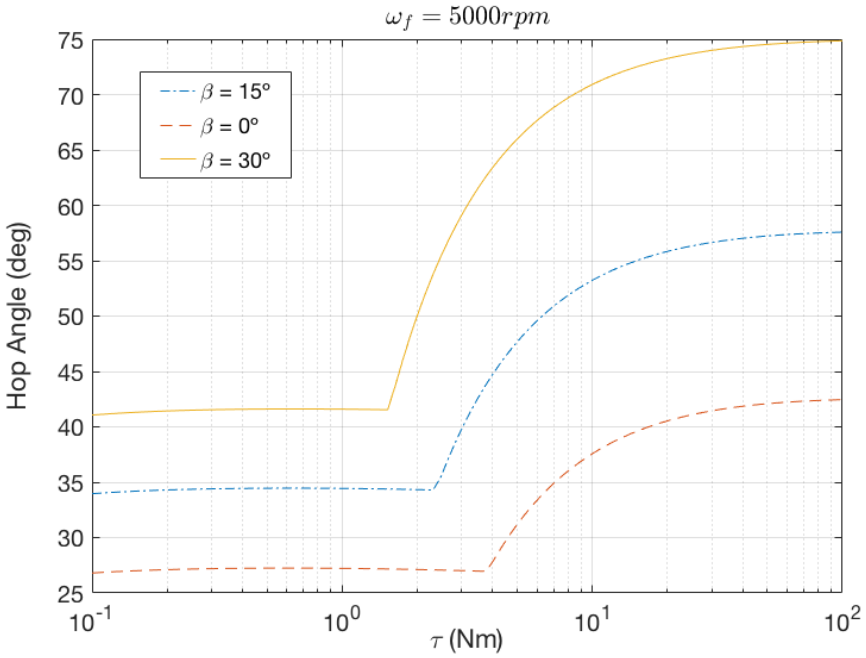


Figure 4.7: Hop angle achieve at the end of the stride phase in terms of the applied braking torque, for an initial flywheel speed of $\omega_f = 5000rpm$ and the parameters listed in Table 2.3.

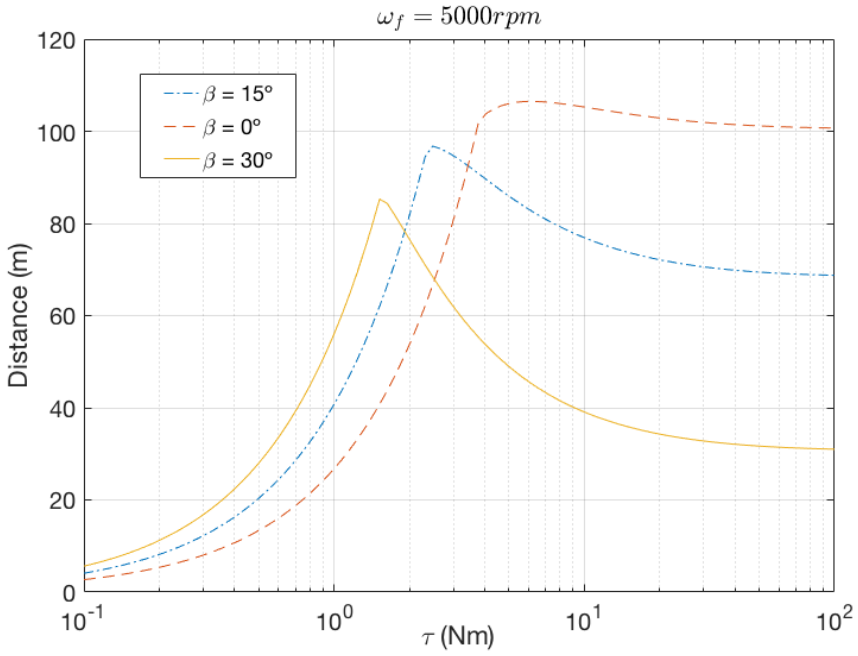


Figure 4.8: Horizontal hop distance achieve by the hopper in terms of the applied braking torque, for a initial flywheel speed of $\omega_f = 5000rpm$ and the parameters listed in Table 2.3.

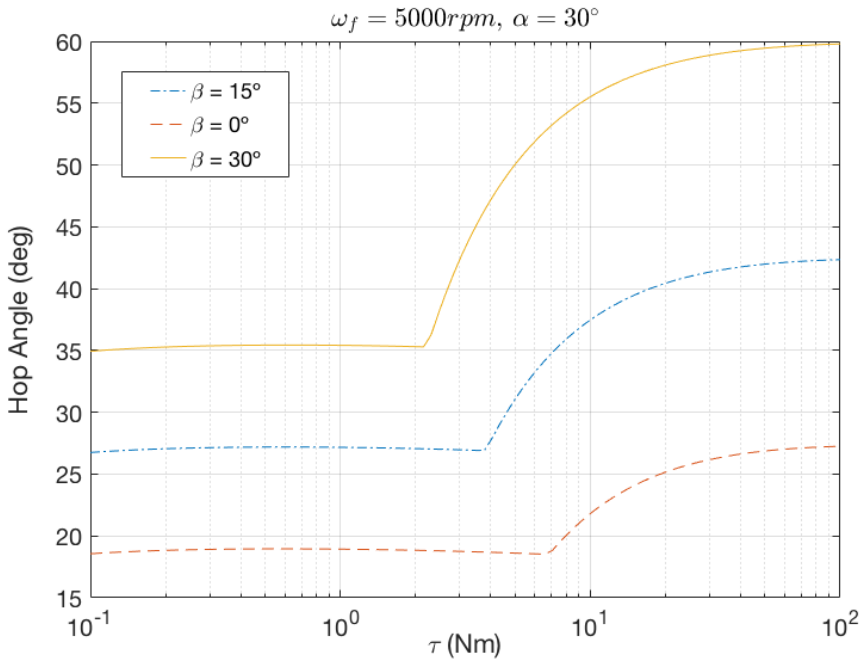


Figure 4.9: Hop angle achieved at the end of the stride phase as function of the applied braking torque, for an initial flywheel speed of $\omega_f = 5000rpm$ and a spike angle of $30$ degrees.

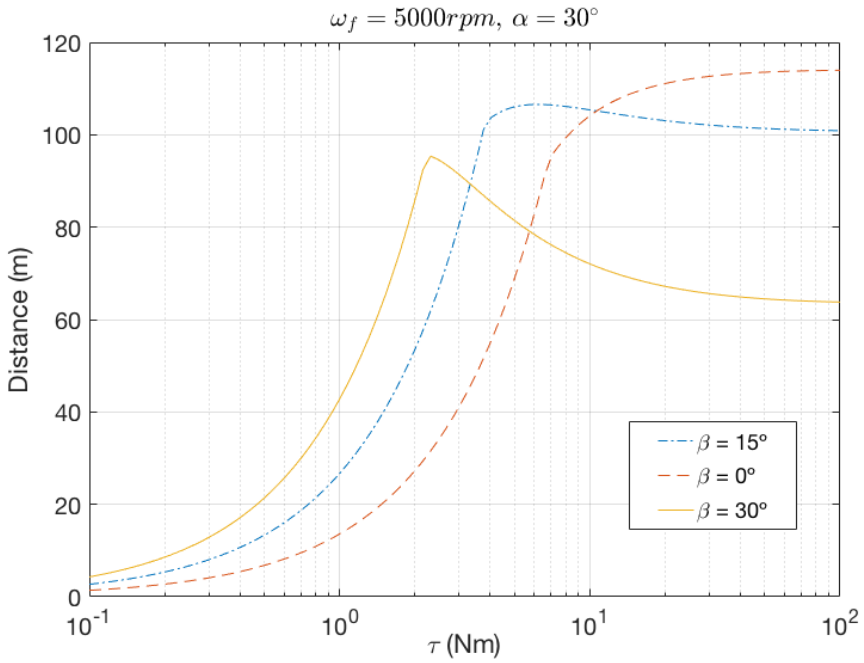


Figure 4.10: Horizontal hop distance achieved by the hopper as function of the applied braking torque, for a initial flywheel speed of $\omega_f = 5000rpm$ and a spike angle of $30$ degrees.

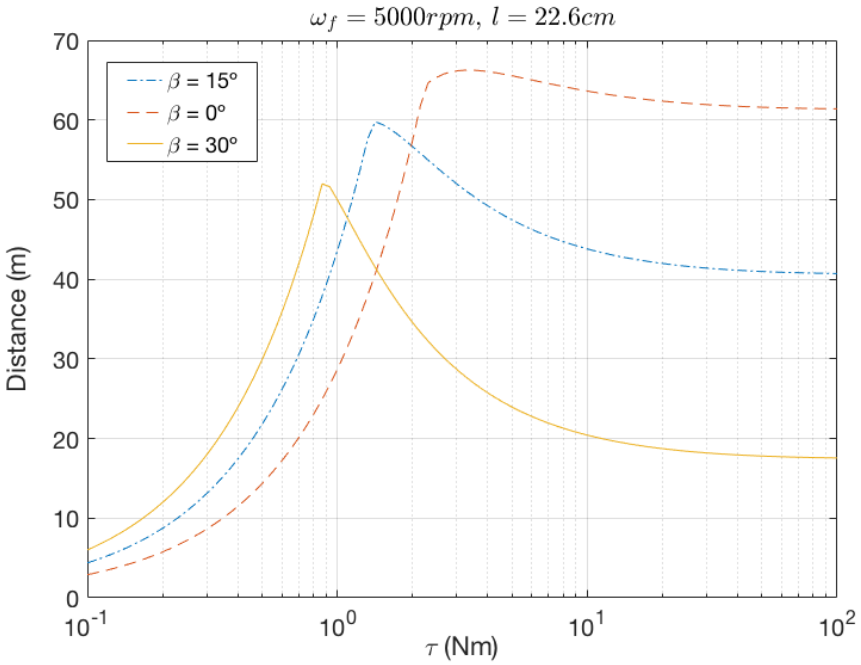


Figure 4.11: Horizontal hop distance achieved by the hopper as function of the applied braking torque, for a initial flywheel speed of $\omega_f = 5000rpm$ and a spike length of $l = 22.6cm$.

## 4.3 Proposed New Applications for the Hopper

Here the proposed innovative and new configurations for the mobility hopper are described. They result from the analysis performed throughout the previous chapters and the simulations obtained. To the best of the author's knowledge, no preexisting proposals, published papers or developed projects in the low-gravity planetary exploration field have suggested or studied the configuration and ideas proposed in this section.

The proposed configuration consists on a spike assembly that can varies its length ($l$) and angle ($\alpha$) prior to the actuation of the flywheels, and that has an internal damping mechanism for energy absorption and dissipation through spike retraction upon collision, during the landing phase. The proposed ideas present a potential contribution for the hopping initiation, tumbling motion and landing phase.

Although the application of the proposed spikes configuration represents an additional sub-system, and could require a more complex actuation control and motion planning, the benefits of this implementation are considerable. The developed proposed applications must favour a effective, simple and robust mechanism.

The benefits of such implementations include better adaptability to the uneven and irregular terrain, characteristic of the Small Bodies surface. Higher control over the hopping angle. An important trade-off solution between the capability of overcoming obstacles (i.e longer spikes), but still with maximized efficiency for the usual hops (i.e. shorter spikes). And an important contribution for the landing phase through dissipation upon impact.

In order to prepare and control the hopper for the impact upon landing, as a result of the selected strategy of attitude control during the flight phase, the proposed configuration and mechanism is allowed to be applied exclusively to the four bottom spikes of the rover instead of the all eight, or even only to the bottom front spikes (i.e. stance spikes). However, if no attitude control strategy is used the proposed applications can be implemented in all eight spikes, with the potential cost of additional actuators.

The mechanical system and actuators for the implementation of the proposed new configurations is left for future work.

### 4.3.1 Variable spike angle

As previously concluded, for the preferred high torque brake of the flywheel, the stride phase duration will be very short. So any desired adjustment to the hopping angle will be slightly modified during this phase, if a constant braking torque is applied, or not modified at all if an instantaneous brake is applied. Plus, high torque mechanical brakes are desired to perform longer and efficient hops, which also allows the main variable input of the flywheels to be its angular speed prior to the brake. Hence, an adjustment of the spike angle ($\alpha$) to adapt to the surface inclination and torque applied, prior to actuation of the brake, presents an advantage to the hopping performance, as supported by the simulation results in Section 4.2. Facing different surface inclinations through the hopper's mobility operations, this provides the possibility of always approximate the hopping angle to $45^{\circ}$ by adjusting the spike angle $\alpha$, obtaining a maximized hop distance, as shown in Equations 3.34, 4.4, and 3.52. Equally sustained by the simulation

results in Figures 4.9 and 4.10.

This application of variable angle spikes, also enables the change of the hopping angle for a controlled value different than $45°$. Representing an advantage for dealing with difficult obstacles from the irregular terrain, or as example, to get out of craters where a wider hopping angle is desired to perform stiffer hops, with a higher ballistic trajectory line.

As a simplistic control approach, some fixed angle positions can be defined for commonly useful angles.

### 4.3.2 Variable spike length

As discussed and determined by previous studies [47], a longer spike configuration facilitates tumbling and hopping over large rocks or obstacles. However, shorter spikes provide a higher actuation efficiency from the flywheel to the hopper, as showed by Equation 3.19 that the efficiency is given by the ratio of the flywheel's inertia and the hopper's inertia about the spike tip, which is quadratically dependable on the spikes' length. Shorter spikes, as the ones used on the Hedgehog rover [32], also allow longer hop distances achieved, as supported by the simulations results (see Figures 4.11 and 4.8). This shows the interest of implementing spikes with a variable length configuration. Working as a trade-off solution between the regular more efficient hops (i.e. shorter spikes) and the obstacle transverse capability (i.e longer spikes). And in cases of high slipping surfaces (e.g. ice in comets), a complete retraction of the spikes offers greater friction.

It is suggested that the spike length can assume three predefined positions in order to simplify the control. A completely retracted spike position, where the length $l$ from the hopper's center of mass to the spike tip plane would be given roughly by the square facet half-diagonal, as shown in Figure 4.12. For the hopper configuration used throughout this thesis, that would imply a $l \approx 11cm$. Adopt an intermediate position, where the spike length would take its usual and more hop efficient position, used and determined by Hockman et al. [32] for the Hedgehog as $l = 16.8cm$. And finally, a fully stretched length of spike position. Applying a specific spike size of approximately twice the adopted by the Hedgehog, which would represent a length of $l = 22.6cm$.

The intermediate position would be defined as the spike's regular length to perform its operations and mobility. From there it could adjust to one of the other two aforementioned positions if the environment and surface conditions, or mission specifics require it. All three possible suggested positions are illustrated in Figure 4.12.

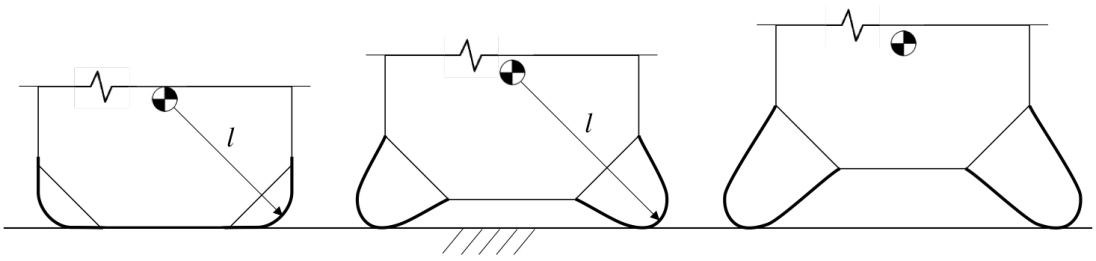


Figure 4.12: Three suggested predefined possible positions for the varying spike's length configuration.

These spike length variability configuration can be also used as advantage for the landing stage, with an internal damping mechanism, to which it represents its potential biggest contribution.

**Internal damping mechanism**

Although the mission profile of this type of mobility rovers is not to land in a specific point but rather a determined area, the collision and subsequent bounces upon landing are nevertheless the biggest source of the motion error [32, 52]. Hence, achieving a softer landing and less rebounds are important to obtain a more precise resting position after the hop is finished.

Working alongside with the spike length variation, an internally installed damping mechanism on each of the bottom spikes can provide an important dissipation of energy upon impact with the surface during landing, reducing the resultant rebound velocity. This could be achieved by applying the spikes' complete stretched length position during the flight phase, which upon impact with the ground would suffer a retraction response through the internal damping mechanism.

Even though, the dynamics and contact analysis were performed considering a flat and homogeneous terrain, the proposed configurations present a possible benefit contribution to a uneven ground, since each spike can adapt individually to the terrain if necessary, reacting better to an irregular surface, contrarily to a rigid rover, specially upon impact with the ground.

### 4.3.3 Additional existent proposed applications

In addition to the innovative proposed applications, other secondary ideas can supplement the proposed implementation. As stated before the 2-DoF actuator configuration like the one used in MINERVA and favored throughout this work, benefits from an uneven distribution of mass, considering it has a defined attitude position for hopping execution. The implementation of small spheres or particles on the end of the bottom spikes would provide a preferred center of mass position closer to its bottom face and at the same time an additional potential energy dissipation mode as suggested by Koenig et al. [46].

# Chapter 5

# Conclusions

## 5.1 Achievements

Throughout this work the main objectives proposed were accomplished. First, through a theoretical overview and literature review, it was possible to determined the more viable mobility configuration and design for the mobility of the hopping rover. Using this configuration a dynamical analysis was performed in a first-order examination.

The determined configuration is based on both the MINERVA rover and the Hedgehog hopper, and consists of a cubic shape with spikes on its corners, and two internally-actuated flywheels for single axis hops. It was selected as the most viable and suitable system. The dynamical analysis of the selected mobility rover allowed to study the hopping motion, considering two different flywheel braking approaches: an impulsive brake for instantaneous momentum transfer to the hopper, and a constant braking torque approach. The results from the simulations support the analytical models that high torques must be favored for maximized hop distance and efficiency.

Through the simulations performed, this work provided proof that for an instantaneous momentum transfer brake the stride phase duration can be assumed zero, and the angle and angular velocity at the hopping instant will be those of the initial state. Analyzing this scenario it was possible to comprehend the influence of the gravity in such mobility systems. It was concluded that such mobility hopper design and configuration is only viable for locomotion in micro-gravity environments.

Through the results obtained from the simulations performed to the constant torque brake, in function of the flywheel initial speed and surface inclination, it was determined the relation and influence of the applied torque values in the hop angle and hop distance achieved, as well as the stride phase duration. And also understand and study the impact of different configurations with alternative spike angles and spike lengths.

The simulations results alongside with the dynamical analysis provided supporting evidences that different spike angles for different surface inclinations provide an interesting application for improved hopping performance. By clearly showing a significant improvement on the hop distance achieved for surface inclination by adjusting the spike angle. They also supported that the a shorter spike config-

uration must be favored for better hop distance performance. The implementation of a variable length spike configuration presents an interesting trade-off solution between the better efficiency and longer hop distance achieved with shorter spikes, and the better transverse capability of bigger obstacles with longer spikes. It also represents an appealing potential improvement to the landing envelope, with the application of an internal damping system on the retractable spikes that provides a energy dissipation mechanism for the impact.

Although the main objective of this thesis was to study the mobility dynamics of a hopping rover for Small Body exploration, this work was able to rise interesting new ideas to be studied and implemented in this type of hopper's configuration.

Even though, the focus of this investigation is the exploration of Small Solar System Bodies, like comets and asteroids, where we are in the presence of micro-gravity, these new applications proposed in Section 4.3 can be adapted to other space explorations hoppers or landing devices.

## 5.2 Future Work

There are opportunities for future work and improvements to be addressed. First, as an improvement to the work developed, execute a second-order approach to the mobility analysis with the inclusion of potential slipping motions on the hopping initiation. In addition, the implementation of a more complex and realistic model of the contact dynamics is necessary for more precised results. This can be achieved by the use of a Multi-Body-System simulation software [35] or with high-fidelity Digital Elevation Models (DEM) [49]. This would allow to simulate the hopper impacts at different velocities and attitudes upon landing, and obtained a high-reliable reproduction of the expected movements and behaviour of the hopper on the irregular surface.

Considering the conclusions and the resulting new proposed implementations to the spikes' configuration, an extensive possible range for future work is open. Starting by further analyze the impact of the aforementioned applications on the hopper's motion and operation. It is suggested the study and develop of mechanism possibilities for the implementation of the presented ideas, which must favour a effective, simple and robust system. Additionally, the test and validation of such mechanisms viability and performance on the complex surface model should also be performed.

Further on, the possibility to develop a CAD prototype with the selected design and mobility configurations, including the implemented variable in angle and length spikes. And in a second level of the project development and testing, conduct experiments to a constructed prototype in small body emulated conditions.

The overall objectives of this master's thesis were achieved and important potential new implementations to the hopper's mobility system emerged. Leaving space and a opportunity for further development and study of this work.

# Bibliography


[1] NASA Solar System Exploration, 2020. URL https://solarsystem.nasa.gov/asteroids-comets-and-meteors/overview/.

[2] R. Z. Sagdeev and A. V. Zakharov. Brief history of the Phobos mission. *Nature, Nature Publishing-Group*, 341(6243):581–585, 1989.

[3] J. I. Lunine, G. Neugebauer, and B. M. Jakosky. Infrared observations of Phobos and Deimos from Viking. *Journal of Geophysical Research*, 87(B12):10297, 1982.

[4] S. Ulamec, V. Kucherenko, J. Biele, A. Bogatchev, A. Makurin, and S. Matrossov. Hopper concepts for small body landers. *Advances in Space Research*, 47(3):428–439, 2011.

[5] A. C. Levasseur-Regourd, J. L. Bertaux, R. Dumont, M. Festou, R. H. Giese, F. Giovane, P. Lamy, J. M. Le Blanc, A. Llebaria, and J. L. Weinberg. Optical probing of comet Halley from the Giotto spacecraft. *Nature, Nature Publishing Group*, 321:341–344, 1986.

[6] M. F. A'Hearn, M. J. Belton, W. A. Delamere, J. Kissel, K. P. Klaasen, L. A. McFadden, K. J. Meech, H. J. Melosh, P. H. Schultz, J. M. Sunshine, P. C. Thomas, J. Veverka, D. K. Yeomans, M. W. Baca, I. Busko, C. J. Crockett, S. M. Colins, M. Desnoyer, C. A. Eberhardy, C. M. Ernst, T. L. Farnham, L. Feaga, O. Groussin, D. Hampton, S. I. Ipatov, J. Y. Li, D. Lindler, C. M. Lisse, N. Mastrodemos, W. M. Owen, J. E. Richardson, D. D. Wellnitz, and R. L. White. Deep Impact: Excavating comet Tempel 1. *Science, AAAS*, 310(5746):258–264, 2005.

[7] D. Brownlee. The stardust mission: Analyzing samples from the edge of the solar system. *Annual Review of Earth and Planetary Sciences*, 42:179–205, 2014.

[8] F. Capaccioni, A. Coradini, G. Filacchione, S. Erard, G. Arnold, P. Drossart, M. C. De Sanctis, D. Bockelee-Morvan, M. T. Capria, F. Tosi, C. Leyrat, B. Schmitt, E. Quirico, P. Cerroni, V. Mennella, A. Raponi, M. Ciarniello, T. McCord, L. Moroz, E. Palomba, E. Ammannito, M. A. Barucci, G. Bellucci, J. Benkhoff, J. P. Bibring, A. Blanco, M. Blecka, R. Carlson, U. Carsenty, L. Colangeli, M. Combes, M. Combi, J. Crovisier, T. Encrenaz, C. Federico, U. Fink, S. Fonti, W. H. Ip, P. Irwin, R. Jaumann, E. Kuehrt, Y. Langevin, G. Magni, S. Mottola, V. Orofino, P. Palumbo, G. Piccioni, U. Schade, F. Taylor, D. Tiphene, G. P. Tozzi, P. Beck, N. Biver, L. Bonal, J. P. Combe, D. Despan, E. Flamini, S. Fornasier, A. Frigeri, D. Grassi, M. Gudipati, A. Longobardo, K. Markus, F. Merlin, R. Orosei, G. Rinaldi, K. Stephan, M. Cartacci, A. Cicchetti, S. Giuppi, Y. Hello, F. Henry,

S. Jacquinod, R. Noschese, G. Peter, R. Politi, J. M. Reess, and A. Semery. The organic-rich surface of comet 67P/Churyumov-Gerasimenko as seen by VIRTIS/Rosetta. *Science, American Association for the Advancement of Science*, 347(6220), 2015.

[9] J. Biele and S. Ulamec. Capabilities of Philae, the Rosetta Lander. *Space Science Reviews, Springer Science&Business Media*, 138(1-4):275–289, 2008.

[10] R. Roll and L. Witte. ROSETTA lander Philae: Touch-down reconstruction. *Planetary and Space Science*, 125:12–19, 2016.

[11] M. J. Belton, J. Veverka, P. Thomas, P. Helfenstein, D. Simonelli, C. Chapman, M. E. Davies, R. Greeley, R. Greenberg, J. Head, S. Murchie, K. Klaasen, T. V. Johnson, A. McEwen, D. Morrison, G. Neukum, F. Fanale, C. Anger, M. Carr, and C. Pilcher. Galileo encounter with 951 Gaspra: First pictures of an asteroid. *Science*, 257(5077):1647–1652, 1992.

[12] J. Veverka, B. Farquhar, M. Robinson, P. Thomas, S. Murchie, A. Harch, P. G. Antreasian, S. R. Chesley, J. K. Miller, W. M. Owen, B. G. Williams, D. Yeomans, D. Dunham, G. Heyler, M. Holdridge, R. L. Nelson, K. E. Whittenburg, J. C. Ray, B. Carcich, A. Cheng, C. Chapman, J. F. Bell, M. Bell, B. Bussey, B. Clark, D. Domingue, M. J. Gaffey, E. Hawkins, N. Izenberg, J. Joseph, R. Kirk, P. Lucey, M. Malin, L. McFadden, W. J. Merline, C. Peterson, L. Prockter, J. Warren, and D. Wellnitz. The landing of the NEAR-Shoemaker spacecraft on asteroid 433 Eros. *Nature, Macmillan Magazines Ltd*, 413(6854):390–393, 2001.

[13] M. Yoshikawa, J. Kawaguchi, and A. Fujiwara. Hayabusa Sample Return Mission. *Asteroids IV, University of Arizona Press*, pages 397–418, 2015.

[14] T. Yoshimitsu, T. Kubota, and I. Nakatani. MINERVA rover which became a small artificial solar satellite. *20th Annual AIAA/USU Conference on Small Satellites*, 2006.

[15] T. Morota, S. Sugita, Y. Cho, M. Kanamaru, E. Tatsumi, N. Sakatani, R. Honda, N. Hirata, H. Kikuchi, M. Yamada, Y. Yokota, S. Kameda, M. Matsuoka, H. Sawada, C. Honda, T. Kouyama, K. Ogawa, H. Suzuki, K. Yoshioka, M. Hayakawa, N. Hirata, M. Hirabayashi, H. Miyamoto, T. Michikami, T. Hiroi, R. Hemmi, O. S. Barnouin, C. M. Ernst, K. Kitazato, T. Nakamura, L. Riu, H. Senshu, H. Kobayashi, S. Sasaki, G. Komatsu, N. Tanabe, Y. Fujii, T. Irie, M. Suemitsu, N. Takaki, C. Sugimoto, K. Yumoto, M. Ishida, H. Kato, K. Moroi, D. Domingue, P. Michel, C. Pilorget, T. Iwata, M. Abe, M. Ohtake, Y. Nakauchi, K. Tsumura, H. Yabuta, Y. Ishihara, R. Noguchi, K. Matsumoto, A. Miura, N. Namiki, S. Tachibana, M. Arakawa, H. Ikeda, K. Wada, T. Mizuno, C. Hirose, S. Hosoda, O. Mori, T. Shimada, S. Soldini, R. Tsukizaki, H. Yano, M. Ozaki, H. Takeuchi, Y. Yamamoto, T. Okada, Y. Shimaki, K. Shirai, Y. Iijima, H. Noda, S. Kikuchi, T. Yamaguchi, N. Ogawa, G. Ono, Y. Mimasu, K. Yoshikawa, T. Takahashi, Y. Takei, A. Fujii, S. Nakazawa, F. Terui, S. Tanaka, M. Yoshikawa, T. Saiki, S. Watanabe, and Y. Tsuda. Sample collection from asteroid (162173) Ryugu by Hayabusa2: Implications for surface evolution. *Science, American Association for the Advancement of Science*, 368(6491):654–659, 2020.

[16] Y. Tsuda, T. Saiki, F. Terui, S. Nakazawa, M. Yoshikawa, and S. ichiro Watanabe. Hayabusa2 mission status: Landing, roving and cratering on asteroid Ryugu. *Acta Astronautica*, 171(January): 42–54, 2020.

[17] T. M. Ho, V. Baturkin, C. Grimm, J. T. Grundmann, C. Hobbie, E. Ksenik, C. Lange, K. Sasaki, M. Schlotterer, M. Talapina, N. Termtanasombat, E. Wejmo, L. Witte, M. Wrasmann, G. Wübbels, J. Rößler, C. Ziach, R. Findlay, J. Biele, C. Krause, S. Ulamec, M. Lange, O. Mierheim, R. Lichtenheldt, M. Maier, J. Reill, H. J. Sedlmayr, P. Bousquet, A. Bellion, O. Bompis, C. Cenac-Morthe, M. Deleuze, S. Fredon, E. Jurado, E. Canalias, R. Jaumann, J. P. Bibring, K. H. Glassmeier, D. Hercik, M. Grott, L. Celotti, F. Cordero, J. Hendrikse, and T. Okada. MASCOT—The Mobile Asteroid Surface Scout Onboard the Hayabusa2 Mission. *Space Science Reviews*, 208(1-4):339–374, 2017.

[18] M. Pavone, J. C. Castillo-Rogez, A. Frick, J. A. Hoffman, and I. A. Nesnas. Spacecraft / Rover Hybrids for the Exploration of Small Solar System Bodies Small Bodies Exploration. Technical report, NASA NIAC Phase II Study, 2017.

[19] S. Montminy, E. Dupuis, and H. Champliaud. Mechanical design of a hopper robot for planetary exploration using SMA as a unique source of power. *Acta Astronautica*, 62(6-7):438–452, 2008.

[20] JPL. Physical Data & Dynamical Constants. URL `https://ssd.jpl.nasa.gov/?phys{_}data`.

[21] Y. Nakamura, S. Shimoda, and S. Shoji. Mobility of a Microgravity Rover using Internal Electro-Magnetic Levitation. *Proceedings - IEEE International Conference on Robotics and Automation*, (23):301–316, 2000.

[22] R. A. Lindemann and C. J. Voorhees. Mars Exploration Rover Mobility Assembly Design, Test and Performance. *Conference Proceedings - IEEE International Conference on Systems, Man and Cybernetics*, 1:450–455, 2005.

[23] S. F. N. Morea. The Lunar Roving Vehicle - Historical Perspective. *Proceedings of the 2nd Conference on Lunar Bases and Space Activities*, 1992. URL `http://library1.nida.ac.th/termpaper6/sd/2554/19755.pdf`.

[24] R. Jones and B. Wilcox. The MUSES CN rover and asteroid exploration mission. *22nd International Symposium on Space Technology and Science*, pages 2403–2410, 2000. URL `http://trs-new.jpl.nasa.gov/dspace/handle/2014/14406`.

[25] Y. Yuguchi, W. F. Ribeiro, K. Nagaoka, and K. Yoshida. Experimental Evaluation of Gripping Characteristics Based on Frictional Theory for Ground Grip Locomotive Robot on an Asteroid. *Proceedings - IEEE International Conference on Robotics and Automation*, (June):2822–2827, 2015.

[26] E. Hand. Philae probe makes bumpy touchdown on a comet. *Science, AAAS*, 346(6212):900–901, 2014.

[27] B. Hockman and M. Pavone. Traversability of Hopping Rovers on Small Solar System Bodies. *Stanford University*, 2016. URL http://asl.stanford.edu/wp-content/papercite-data/pdf/Hockman.Pavone.ISAIRAS18.pdf.

[28] S. Shimoda, A. Wingart, K. Takahashi, T. Kubota, and I. Nakatani. Microgravity Hopping Robot with Controlled Hopping and Landing Capability. *IEEE International Conference on Intelligent Robots and Systems*, 2003.

[29] J. Burdick and P. Fiorini. Minimalist Jumping Robots for Celestial Exploration. *The International Journal of Robotics Research, SAGE Publications*, 22(7-8):653–674, 2003.

[30] S. Shimoda, T. Kubota, and I. Nakatani. New Mobility System Based on Elastic Energy under Microgravity. *IEEE International Conference on Intelligent Robots and Systems*, (May):2296–2301, 2002.

[31] M. Gajamohan, M. Merz, I. Thommen, and R. D'Andrea. The Cubli: A Cube that can Jump up and Balance. *IEEE International Conference on Intelligent Robots and Systems*, pages 3722–3727, 2012. URL https://www.youtube.com/watch?v=n{_}6p-1J551Y.

[32] B. J. Hockman, A. Frick, R. G. Reid, I. A. Nesnas, and M. Pavone. Design, Control, and Experimentation of Internally-Actuated Rovers for the Exploration of Low-gravity Planetary Bodies. *Journal of Field Robotics*, 34(1):5–24, 2017.

[33] F. Herrmann, S. Kuß, and B. Schäfer. Low-Gravity Planetary Body Exploration. *Earth*, (April), 2011.

[34] T. Kubota, K. Takahashi, S. Shimoda, T. Yoshimitsu, and I. Nakatani. Locomotion Mechanism of Intelligent Unmanned Explorer for Deep Space Exploration. *Studies in Computational Intelligence, Springer*, 192:11–26, 2009.

[35] A. Gibbesch, R. Krenn, F. Herrmann, B. Sch, B. Rebele, and T. Diedrich. Multi-Body System and Contact Simulation within the Design Development of Planetary Surface Exploration Systems. *Proceedings. ISAIRAS*, pages 322–329, 2010.

[36] T. Yoshimitsu, T. Kubota, T. Adachi, and Y. Kuroda. Advanced robotic system of hopping rovers for small solar system bodies. *International Symposium on Artificial Intelligence, Robotics and Automation in Space*, (1):3–7, 2012. URL http://robotics.estec.esa.int/i-SAIRAS/isairas2012/Papers/Session6A/06A{_}01{_}yoshimitsu.pdf.

[37] S. Shimoda, T. Kubota, and I. Nakatani. New mobility system based on elastic energy under microgravity. *Proceedings - IEEE International Conference on Robotics and Automation*, 3(August 2014):2296–2301, 2002.

[38] K. Yoshida. The Jumping Tortoise: A Robot Design for Locomotion on Micro Gravity Surface. *Proceedings of the 5th International Symposium on Artifical Intelligence, Robotics and Automation in Space*, 1999:705–707, 1999.

[39] T. Yoshimitsu, T. Kubota, I. Nakatani, T. Adachi, and H. Saito. Micro-hopping robot for asteroid exploration. *Acta Astronautica*, 52(2-6):441–446, 2003.

[40] C. Lange, T. M. Ho, C. D. Grimm, J. T. Grundmann, C. Ziach, and R. Lichtenheldt. Exploring small bodies: Nano- and microlander options derived from the Mobile Asteroid Surface Scout. *Advances in Space Research*, 62(8):2055–2083, 2018.

[41] J. Reill, H.-J. Sedlmayr, S. K. P. Neugebauer, M. Maier, A. Gibbesch, B. Schäfer, and A. Albu-Schaeffer. Development of a Mobility Drive Unit for Low Gravity Planetary Body Exploration. *ASTRA - 12th ESA Symposium on Advanced Space Technologies for Robotics and Automation*, 2013. URL `http://elib.dlr.de/86421/`.

[42] D. Bender. *Storing Energy, Chapter 10 – Flywheels*. Elsevier Inc., 2016.

[43] C. D. Grimm, J. T. Grundmann, J. Hendrikse, C. Lange, C. Ziach, and T. M. Ho. From idea to flight - A review of the Mobile Asteroid Surface Scout (MASCOT) development and a comparison to historical fast-paced space programs. *Progress in Aerospace Sciences, Elsevier*, 104(November): 20–39, 2019.

[44] M. Pavone, J. C. Castillo-Rogez, I. A. Nesnas, J. A. Hoffman, and N. J. Strange. Spacecraft/Rover Hybrids for the Exploration of Small Solar System Bodies. *IEEE Aerospace Conference Proceedings*, 2013.

[45] R. Allen, M. Pavone, C. McQuin, I. A. Nesnas, J. C. Castillo-Rogez, T. N. Nguyen, and J. A. Hoffman. Internally-Actuated Rovers for All-Access Surface Mobility: Theory and Experimentation. *Proceedings - IEEE International Conference on Robotics and Automation*, pages 5481–5488, 2013.

[46] A. W. Koenig, M. Pavone, J. C. Castillo-Rogez, and I. A. Nesnas. A Dynamical Characterization of Internally-Actuated Microgravity Mobility Systems. *Proceedings - IEEE International Conference on Robotics and Automation*, pages 6618–6624, 2014.

[47] R. G. Reid, L. Roveda, I. A. D. Nesnas, and M. Pavone. Contact Dynamics of Internally-Actuated Platforms for the Exploration of Small Solar System Bodies. *International Symposium on Artificial Intelligence, Robotics and Automation in Space*, pages 1–9, 2014.

[48] T. McGeer. *Passive dynamic walking*. PhD thesis, School of Engineering Simon Fraser University, 1990.

[49] S. Van wal. *High-Fidelity Simulation of Small-Body Lander / Rover Spacecraft*. PhD thesis, University of Colorado, 2018.

[50] S.-W. Kim. *Contact dynamics and force control of flexible multi-body systems*. PhD thesis, McGill University, Montreal, 1999. URL `http://www.collectionscanada.gc.ca/obj/s4/f2/dsk1/tape4/PQDD{_}0035/NQ64588.pdf`.

[51] G. Gilardi and I. Sharf. Literature survey of contact dynamics modelling. *Mechanism and Machine Theory*, 37(10):1213–1239, 2002.

[52] B. Hockman and M. Pavone. Stochastic Motion Planning for Hopping Rovers on Small Solar System Bodies. *Robotics Research*, pages 877–893, 2017.

[53] X. Li, A. K. Sanyal, R. R. Warier, and D. Qiao. Landing of hopping rovers on Irregularly-shaped small bodies using attitude control. *Advances in Space Research, Elsevier*, 65(11):2674–2691, 2020.

[54] S. K. Saha, P. Fiorini, and S. V. Shah. Landing Mechanisms for Hopping Robots : Considerations and Prospects. *Proceedings of the 9th ESA Workshop on Advanced Space Technologies for Robotics and Automation*, (1):1–8, 2006.

[55] G. Wilburn, H. Kalita, and J. Thangavelautham. Development and Testing of an Engineering Model for an Asteroid Hopping Robot. *IAC*, pages 1–9, 2019.

[56] W. J. Stronge. Rigid Body Collisions with Friction. *Proceedings: Mathematical and Physical Sciences*, 1990.

[57] M. Ahmad, K. A. Ismail, and F. Mat. Impact models and coefficient of restitution: A review. *ARPN Journal of Engineering and Applied Sciences*, 11(10):6549–6555, 2016.

[58] O. Montenbruck and E. Gill. *Satellite orbits: models, methods and applications*. Springer Science & Business Media, 2012.